Università Cattolica del Sacro Cuore

Sede di Brescia

Facoltà di Scienze Matematiche, Fisiche e Naturali

Corso di Laurea in Fisica

Tesi di Laurea

TIME-RESOLVED OPTICAL INVESTIGATION OF GOLD NANOSPHERES IMMOBILIZED ON FUNCTIONALIZED SURFACES FOR BIOLOGICAL APPLICATIONS

Relatore:

Prof. Gabriele Ferrini

Candidata:

Giada Bianchetti

Matr. 4104562

Anno Accademico 2014/2015

Al nonno Angelo,
alla nonna Betta
e alla zia Cati

Contents

1 Introduction **4**

1.1 Overview 4

1.2 Outline 5

2 Time-resolved spectroscopy **6**

2.1 Optical Pump & Probe technique 6

2.2 Direct comparison between standard pump & probe experiments and ASOPS . . 7

2.2.1 Working principle of ASOPS 8

2.2.2 Alternative mode of operation: ECOPS technique 10

2.3 Setup scheme 11

2.3.1 Nanoscope 13

2.3.2 Sample's properties 14

2.4 Operating procedures for the setup's setting 17

3 Experimental measurements **19**

3.1 Overview 19

3.1.1 Single nanoparticle's detection 19

3.2 Time-resolved measurements on gold nanospheres 21

3.3 Thermal analysis 23

3.4 Mechanical analysis 26

4 Conclusions and future perspectives **40**

A Fit procedures **42**

A.1 Thermal fit 42

A.2 Mechanical fit 42

B Electronics and devices **44**

B.1 High-speed Photodetector 44

B.1.1 Differential Photodetector: PDB430A 44

C Acronyms **47**

Chapter 1

Introduction

1.1 Overview

Nanotechnology has recently become one of the most exciting forefront fields. A wide variety of nanomaterials, especially nanoparticles with different properties, have found broad application in many kinds of analytical methods. Owing to their small size (normally in the range of 1-100 nm), nanoparticles exhibit unique chemical, physical and electronic properties that are different from those of bulk materials and can be used to develop and improve spectroscopic techniques. By operating in the nanoscale realm, nanotechnology offers a wide range of tools and applications also in biological fields. Near-term applications include fluorescent biological labels [4]-[5], drug and gene delivery [6]-[7], biodetection of pathogens [8] and thermal therapy [9].

We are now interested in the analysis of the thermomechanical properties of gold nanoparticles immobilized with different concentrations on a functionalized surface through the bond between biotin and streptavidin, which is characterized by high affinity and binding energy. The interest in these complex biomolecular systems is due to their analogy with the real world of living cells, that can be investigate using nanoscale constructs.

In this context we develop the work of this thesis, whose aim is to study how optical properties, especially transmission, of gold nanospheres are influenced and altered by the presence of these biochemical bonds.

1.2 Outline

The work is organized as follows. Chapter 2 introduces the basic concepts of time-resolved spectroscopy, illustrating the *pump & probe* technique, with the working principle of ASyncrhronous Optical Sampling (ASOPS) and Electrically Controlled OPtical Sampling (ECOPS), and the structure of the experimental setup, the nanoscope and sample's properties, followed by the operative procedures. In Chapter 3 is related the measure of thermomechanical dynamics of a single gold nanoparticle immobilized on a functionalized surface. The last chapter presents the conclusions of our work and shows the future perspectives linked to the possible uses of this technique.

Chapter 2

Time-resolved spectroscopy

Time-resolved spectroscopy is the name given to a set of experimental tools that allow to measure time-resolved quantities. Through this method it is possible to probe the thermomechanical properties and dynamics of single particles, in our specific case gold nanospheres immobilized on a functionalized surface through a biochemical bond. To do this kind of analysis is necessary to focus the laser beam on a single nanoparticle, and, then, to perform a time-resolved optical transmission measurement, spanning a time window up to 10 ns by the use of ASynchronous Optical Sampling (ASOPS). First, it is important to introduce the *pump & probe* technique, comparing it with the traditional one, then present the ASOPS system, describing the optical set-up, and, finally, illustrate the optical nanoscope and the samples.

2.1 Optical Pump & Probe technique

Pump & probe spectroscopy is the experimental technique used to evaluate the dynamic of the optical excitations to which the sample is subjected. In fact, this kind of spectroscopy enables to follow in real time vibrational motions coupled to electronic transitions. In this technique, an ultrashort pulsed laser let us to analize physical phenomena with an high temporal resolution and also to obtain impulse of high amplitude even though the amount of mean energy provided is fairly low, thus avoided the risk to damage the sample. The ultrashort pulsed beam is splitted into two components: a stronger beam (pump) is used to excite the sample, generating a non-equilibrium state, whereas a weaker beam (probe) is used to monitor the pump-induced changes in the optical constants of the sample, such as reflectivity or transmission. Measuring variations

of optical features as a function of time delay between the arrival of pump and probe pulses yields information about the relaxation of electronic states in the sample. From the analysis of these results it is possible to retrace its properties, which is the aim of our work.

2.2 Direct comparison between standard pump & probe experiments and ASOPS

There are different possible ways to introduce a delay between the pump pulse and the probe one. A standard method consists in varying the lenght of the probe's path. As represented in Figure 2.1, the movement of a motor-powered translation stage introduces a mechanical delay δx, that implies a variation of 2δx in the optical path of the beam. This mechanical delay is correlated to a time delay δt, given by

$$\delta t = \frac{2\delta x}{c} \quad \text{where} \quad c = 30\ cm/ns \text{ is the speed of light}$$

A severe disadvantage of the conventional approach is the fact that a physical mass needs to be moved to accomplish the time-delay, significantly limiting the scanning speed. In addition, translation stages suffer from alignment error, impeding precise calibration and causing measurement artifacts. Above all that, it would be extremely difficult to keep the correct alignment during the movement of the translation stage because of the diameter of the laser spot focalized on the sample, of the order of few μm.

To solve all these problems connected to the traditional technique, a new method, called *ASOPS*, that stands for ASynchronous Optical Sampling, has been introduced. With this technique, it is possible to obtain a temporal resolution lower then 100 fs in a time window wider than 10 ns, exploiting two ultrafast lasers with offset repetition rates. The time separation between excitation and probe pulse is scanned automatically at a constant rate given by the offset frequency $\Delta\nu$, called *detuning*. Furthermore, the stability of the system is improved as there are no moving mechanics to affect pointing stability or spot sizes.

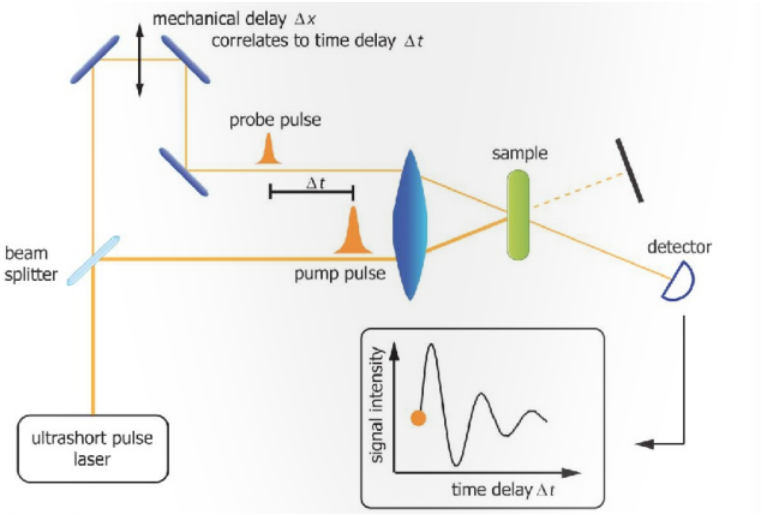

Figure 2.1: Typical pump & probe experiment. The signal from the probe pulses is detected as the mechanical delay line is being scanned. By the relation $\delta t = \frac{2\delta x}{c}$, c being the speed of light, the position change of the mechanical delay line is translated into a change of the time delay between pump and probe pulse.

2.2.1 Working principle of ASOPS

The ASOPS system considered in this work is composed by two pulsed lasers with wavelenght of 780 nm and 1560 nm and pulse width of about 150 fs. The cavity has a repetition rate $\nu_{pump} = 100\,\text{MHz}$ for the pump laser, while probe's one can be expressed as

$$\nu_{probe} = \nu_{pump} - \Delta\nu = 100\,\text{MHz} - \Delta\nu \text{ con } \Delta\nu \ll \nu_{pump} \tag{2.1}$$

Once defined the repetition-rate frequencies of the two lasers, the temporal delay Δt between them will be

$$\Delta t = \left| \frac{1}{\nu_{pump}} - \frac{1}{\nu_{probe}} \right| = \frac{\Delta\nu}{\nu_{probe} \cdot \nu_{pump}} \tag{2.2}$$

Assuming the frequency difference $\Delta\nu \ll \nu$, one obtain

$$\Delta t \approx \frac{\Delta\nu}{\nu_{pump}^2} \tag{2.3}$$

Figure 2.2: Laser sources and ASOPS system

which represents the minimum step between consecutive pulses of pump and probe. For every pulse, the delay increases of a quantity Δt until probe beam finds itself again in coincidence with a pump one after $\frac{1}{\Delta\nu}$. In this way, considering a typical detuning frequency of 1 kHz, the time window for a complete *pump & probe* measurement is

$$t_{window} = \frac{1}{\nu_{pump}} = \frac{1}{100\,\mathrm{MHz}} = 10\,\mathrm{ns} \tag{2.4}$$

The working principle of the detuning is schematically reported in Figure 2.3

The electronic management of the delay between the two laser pulses avoids the problems which characterized the standard *pump & probe* method. Indeed, the generation of temporal delay without a mechanical translation stage avoids the problems relating to the spatial coincidence of the two laser beams. While with the traditional technique the time required to investigate an interval of 10 ns with a temporal resolution of 150 fs is of the order of one hour, with the use of ASOPS the same measurement is settled in 1 ms.[1]
Regarding the maximum delay, the use of ASOPS technique allows to increase it of one order of magnitude, from ns to 10 ns.

[1] Assuming that the measure is realized with a detuning of 1 kHz. Moreover to improve the ratio signal/noise the measurement must be integrated increasing the capturing time up to the order of minutes.

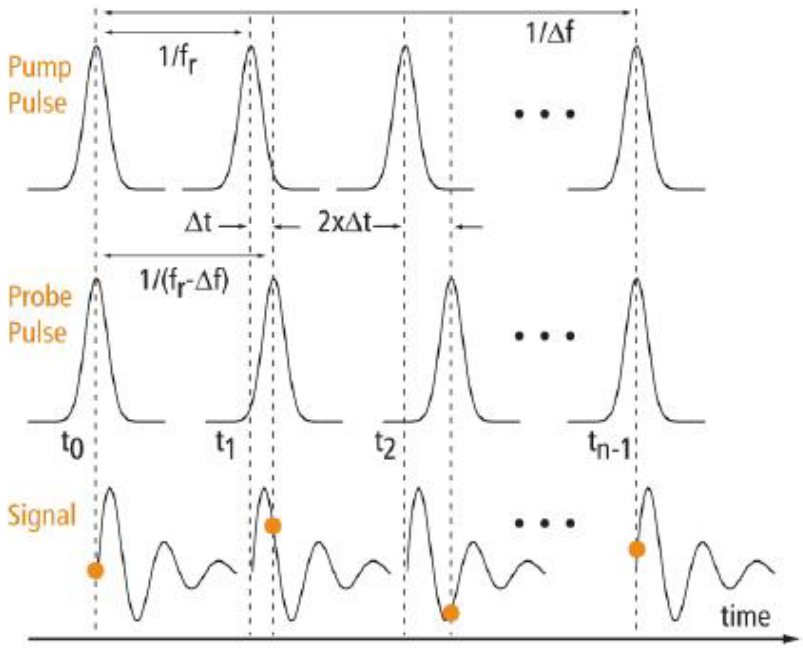

Figure 2.3: Operating principle of the ASOPS technique. In figure is shown the mutual temporal delay between the pump and the probe pulse, defying f_r and $f_r - \Delta f$ respectively. Because of the detuning Δf between the pulses of the two lasers, a progressive temporal delay between them is generated which allows to measure the entire relaxing dynamics of the sample. The image has been taken from the technical manual for the use of ASOPS.

There are several setups to make a pump & probe measure, characterised by the way in which probe pulse interacts with the sample: transmission, reflection or evanescent waves. We are now interested in transmission measurements, a kind of analysis that allows us to examine properties of the nanospheres.

2.2.2 Alternative mode of operation: ECOPS technique

Some experiments may not require scanning the signal throughout the maximal delay range given by

$$\nu_{rep} = 100\,\text{MHz} \quad \Rightarrow \quad \frac{1}{\nu_{rep}} = 10\ ns \tag{2.5}$$

If, for example, one needs only to know the behaviour of the sample during the first 100 ps after excitation, a full scan over the maximal delay range (10 ns) would not be very efficient.

Alternatively, one can realize the adjustable delay between the two lasers by alternating the sign of the offset frequency $\Delta\nu$ on a timescale t_{sweep} much shorter than $\frac{1}{\Delta\nu}$. The use of this

method, called ECOPS, acronym for Electrically Controlled OPtical Sampling, allows to achieve a significantly narrower time window for the measurements.
As showed in Figure 2.4, by alternating the sign of $\Delta\nu$, the delay $\Delta\tau$ between pump pulse and probe pulse can be scanned in both directions.

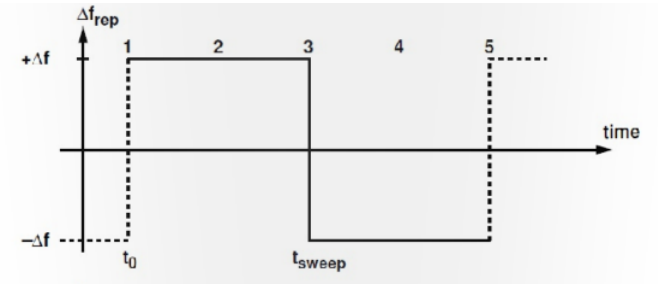

Figure 2.4: Working principle of ECOPS. This technique modulates the repetition rate offset such that the time delay of the probe pulses relative to the pump pulses is modulated in a small time delay region around the time zero point.

In this mode of operation, the maximum time delay, defined $\Delta\tau_{max}$, is determined by the offset frequency $\Delta\nu$ and by the sweep time t_{sweep} as

$$\Delta\tau_{max} = \left[\frac{t_{sweep}}{T_{rep}}\right]\Delta t = \frac{\Delta\nu}{\nu_{rep}}\ t_{sweep} \tag{2.6}$$

where the ratio t_{sweep}/T_{rep} gives the number of pairs of pulses and Δt is the minimum step between consecutive pulses, as defined in Equation 2.3. From this relation, the temporal delay Δt can be written as

$$\Delta t = \frac{\Delta\tau_{max}}{\nu_{rep} \cdot t_{sweep}} \tag{2.7}$$

This procedure can be implemented using the same electronic of ASOPS, so switching between two modes of operation can be easily done without doing any change to the experimental setup itself. In this way, it is possible to scan either the full range up to 10 ns or zoom in the time delay over a range on the order of 10-100 ps.

2.3 Setup scheme

The experimental setup that we will use in our work is schematically reported in Figure 2.5. This setup is conceived for time-resolved optical microscopy measurements on nanostructured

samples. Laser sources, nanoscope and detectors are depicted as black boxes. Mirrors and lens have a characteristic representation and the complete legend is reported below Figure 2.5.

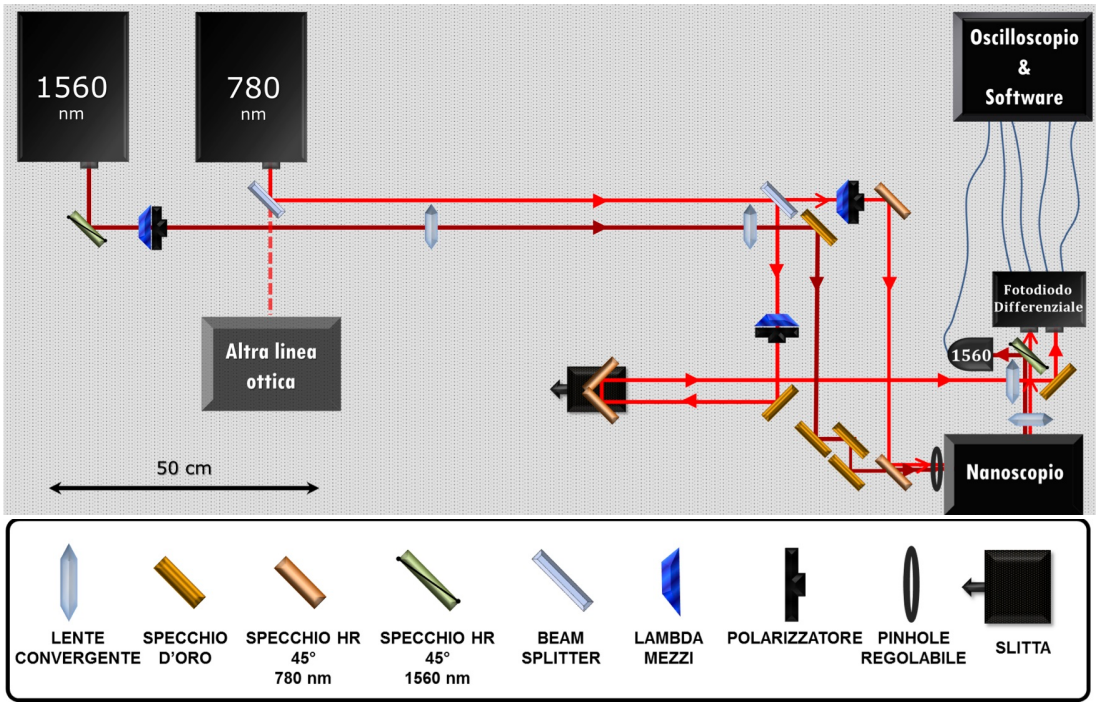

Figure 2.5: Reference experimental setup. This arrangements allows to follow the thermomechanical dynamics of nanostructrured sample, exploiting the pump & probe technique with ASOPS.

To generate the pulses at 1560 nm for our experiments we used a erbium doped fibre laser, guided in the nanoscope through a system of mirrors. An half-wave plate coupled with a polarizer allows to settle the intensity of the beam, while the passage through two convex lenses of focal lenght 40 cm and 20 cm, f_1 and f_2 respectively, forming an expanding telescope, expands the diameter of beam. Before the pump beam enters the nanoscope, it passes through a pinhole of variable radius, then it is detected by a photodetector, labelled as "1560".

The probe beam, at 780 nm, is splitted twice by a 50/50 beam splitter. The first split is necessary to feed an optics line outward of our optical path, while the second one produces two beams at the same wavelenght: *probe beam*, which is transmitted across the beam splitter and, after the passage in a half wave-plate, undergoes a double reflection by two mirrors and enters the nanoscope, and the *reference* one, directly driven to the differential photodetector. A mechanical translation stage[2] supports two mirrors, forming the optical path of the reference line. Varying

[2]Maximum range is 2,5 cm with a resolution of 10 μm

the path of this line, we set the temporal overlapping of the probe beam trasmitted through the sample and the unperturbed one, before entering the photodetector, which is fundamental in order to acquire the difference between these signals.

2.3.1 Nanoscope

The structure of the nanoscope, together with the common path of pump and probe beams and the reference system, is outlined in Figure 2.6. It is composed by four mirrors, two objectives and a CCD camera. After the beam enters the nanoscope, it is reflected by a system of mirrors into a 50X Nikon objective, which focuses the beam on the sample. The divergent beam, transmitted through the sample, is collected by an identical objective, and it is guided to the photodiode.

The advantages of using the nanoscope are:

- The size of probe beam's spot (1 μm) facilitates the detection of objects characterized by dimensions much lower than wavelenght of laser beam. If the distance between two nanoparticles on the sample is similar to the size of laser's spot, it could be easier to identify the single particle focusing the probe beam to the diffraction limit.

- Characterization and spatial control of the position of laser beams.
  By means of the nanoscope, it is possible to retrace the spatial distribution of beams, focus the beam on the xy plane in which the sample lies, and also evaluate the angle of beam with respect to z axis.

- Optimization of beams to perform *pump & probe* measurements.
  It is important to locate the mutual position of beams in order to make them collinear, incident on the sample and directed along the z axis. The probe beam ($\lambda = 780\,\text{nm}$) is focused nearer to the first objective than the pump beam ($\lambda = 1560\,\text{nm}$). This represents a great advantage in the current setup. On the sample, the pump spot is larger than the probe spot. This assure that we are probing an uniformly excited area of the sample.

These features are so important because they allow the correct positioning of beams on the nanospheres, which is necessary to make our measurements. The aim of this work is the analysis

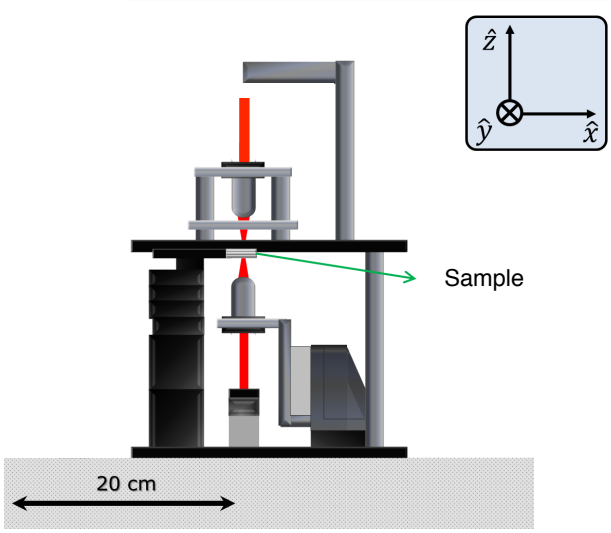

Figure 2.6: Nanoscope's structure and beams' path

of the power transmitted through a single or group of nanoparticles at the position (x_0, y_0) on a surface, defined as

$$P_t = P_i - \sigma_{ext} \cdot I(x_0, y_0) \tag{2.8}$$

where P_i is the incident power on the sample, σ_{ext} is the effective cross section and $I(x_0, y_0)$ is the intensity spatial profile assumed to be Gaussian. So, the second term on the right-hand side represents a power and takes into account both the energy absorbed and scattered by the sample. Therefore, the photodetector gives a signal in terms of voltage and to identify the signal coming from the nanoparticles is necessary to do a sequence of translations, the so-called *raster scan*, that allows to create an image, that represents the beam reconstructed using the nanosphere. Indeed, when the probe beam, whose spot is much bigger than the characteristic size of particles, passes on a nanosphere, the system records a variation of transmitted power given by the convolution of the Gaussian function, corresponding to the beam, and a Dirac Delta function, associated to the particle.

2.3.2 Sample's properties

In this subsection, we want to describe the structure of our sample, which has been realized at *NEST Laboratory*[3] and consists of a sapphire (Al_2O_3) cover slide (diameter 12 mm, thickness 180

[3]National Enterprise for nanoScience and nanoTechnology, Pisa, Italy

μm), on which are litographed Cr/Au 10 nm/100 nm markers, required to localize nanoparticles on the sample, through the Knife-edge technique. Markers' templates are sketched in Figure 2.7 and 2.8.

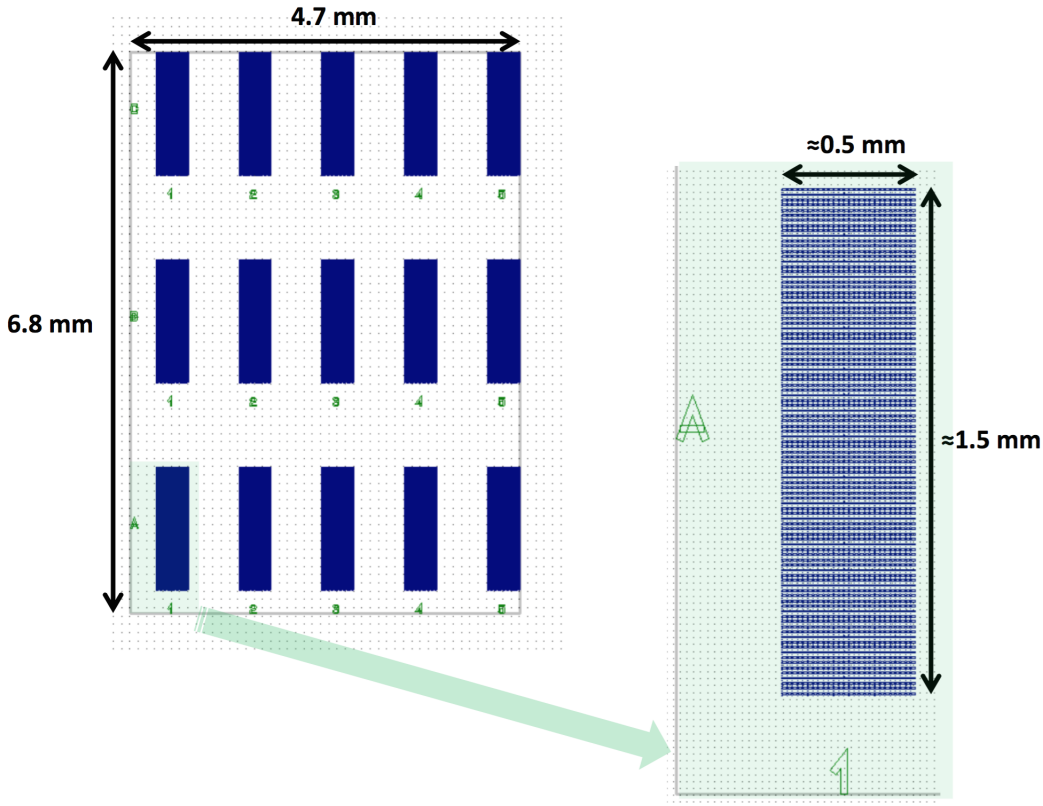

Figure 2.7: Scheme of a template (4,7 mm x 6,8 mm), characterized by macro-areas ($\sim$ 0,5 mm x $\sim$ 1,5 mm), that allow to spot different concentrations of antibody on the same slide

On this substratum, after its functionalization, gold nanospheres have been immobilized, by means of the procedure explained in the following paragraph.

Production method of samples

The functionalization of our samples has been realized at *ICRM-CNR*,[4] by deposition of streptavidin conjugated gold nanoparticles[5] (diameter 40 nm) on the substratum. We are now going to explain the procedure followed to coat the slides. After 15 minutes of oxygen plasma treatment, sapphire substratum were immersed for 30 minutes in a 0,9 M ammonium sulfate solution (half volume of H_2O, half volume of NH_4SO_4) containing poly (DMA-co-NAS-co-MAPS)[6] at

[4]Istituto di Chimica del Riconoscimento Molecolare-Consiglio Nazionale delle Ricerche, Milan, Italy
[5]Made by Cytodiagnostics, Burlington, Ontario, Canada
[6]For the synthesis of copoly refer to [10]

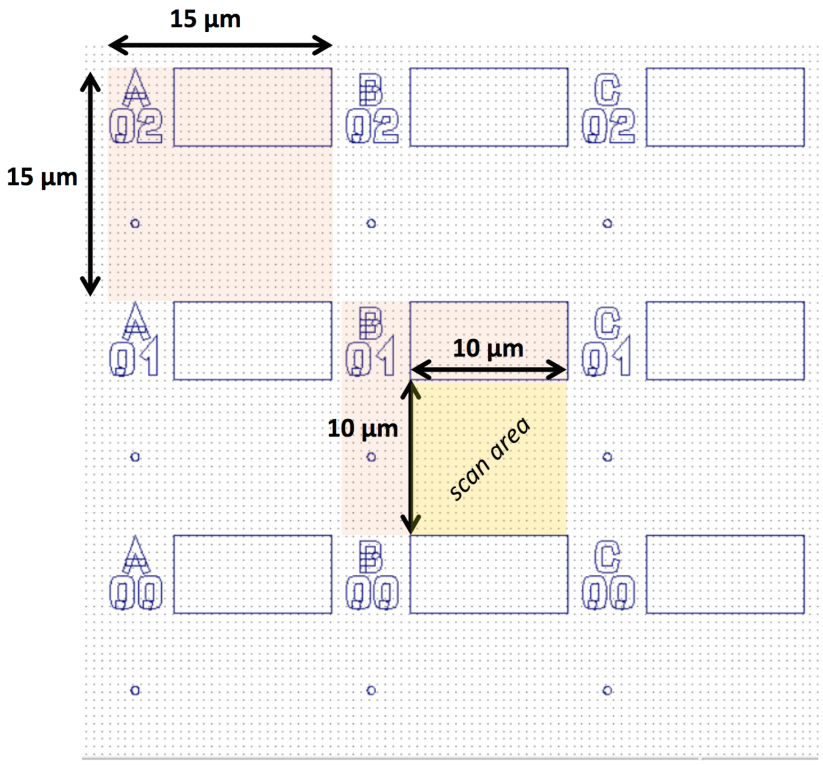

Figure 2.8: Each marker that identifies a macro-area is divided in cells (15 μm x 15 μm), named with a letter and a number and characterized by a scan area of 10 μm x 10 μm, a gold edge and a dot (diameter 500 nm), useful to identify the correct position of particles on the sample

1% w/v concentration.[7] The slides were left for 20 minutes immersed in the polymer solution and then rinsed with water, dried with nitrogen and finally cured under vacuum at 80° for 15 minutes. The last passage, named *curing*, in addition to dry the sample, facilitates the creation of a strong bond between the polymer and the surface. To demonstrate the functionalization of nanoparticles with streptavidin, biotinylated antibody was patterned on sapphire slides[8] coated with polymer. The antibody was diluited in Phosphate Buffered Saline (PBS) with four different concentrations and the solution was spotted on the sample. The slides were placed in a humid chamber immediately after the spotting and stored overnight at room temperature. After immobilization, the residual active esters on the slides were blocked with a blocking solution (ethanolamine) for 1 hour, washed with water and dried by a stream of nitrogen. The spotted slides were then incubated with a solution of gold nanospheres conjugated with streptavidin

[7]The 1% concentration, expressed through the ratio weight/volume, means that there is 1 g of solute for 100 ml of solution

[8]Made by means of SciFlexArrayer S5 spotter from Scienion (Berlin, Germany). The diameter of the spot is about 150 μm

at different concentrations for 1 hour, washed with the Washing Buffer for 10 minutes under stirring and finally rinsed with water and dried with nitrogen.

2.4 Operating procedures for the setup's setting

In this section we summarize the preliminary procedures to perform measurements by means of the nanoscope. To obtain a measure as accurate as possible, it is necessary that both pump and probe beams are parallel and coaxial. In order that all these conditions are respected, it is essential to follow several procedures:

- **Alignment of beams**

  Pump and probe beams must enter the nanoscope collinearly and spatially overlapped, because spatial coincidence is required.

- **Nanoscope's optimization**

  The core of nanoscope consists of two 50X objective. Their first task is to focus the two beams on the sample's plane, while the second is to collect them and drive them to the photodetector. There are two basic rules to respect. First of all, the two objectives must be colllinear and their focal points must overlap.

- **Research of the minimum waist**

  Once we get the correct setting of the objectives, our aim is to place the sample at the minimum waist of the probe beam. To do this, we use the so-called *Knife-edge* technique.[9]

- **Positioning on the single nanosphere**

  The programme "SPM Control" allows to do a scan of the sample, obtaining the *imaging* of the beam. Let us consider how to perform an imaging of a square area. Thanks to a command, namely *raster scan*, the SPM software runs a set of translations in the xy plane. These displacements follow a precise path, while the photodiode records the transmitted optical power at each point of the scan. The photodiode output voltage defines the greyscale of each single pixel that creates the image. We specify that the greyscale that composes the image depends on the Data Acquisition System. The maximum voltage value defines the scale on which the total number of grey are assigned. When we perform a scan

[9] More details in [11] and [12]

we get light and dark areas. The dark areas indicate that the beam is not transmitted, as reported in Figure 2.9.

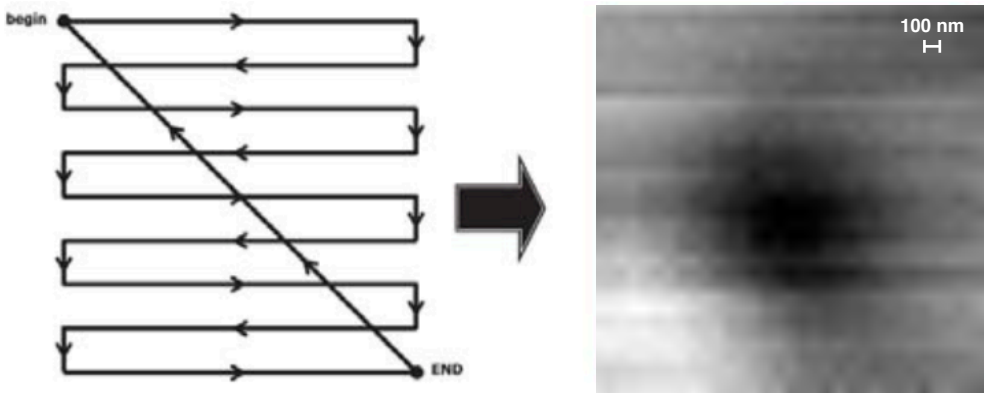

Figure 2.9: On the left, the total displacement realized by a raster scan. On the right, an example of a digital image obtained scanning a 2000x2000 nm area with a 32x32 pixel resolution, in which we can identify the signal given by the presence of a nanoparticle.

The path illustrated is completed through different steps. The speed of the scan and the acquisition delay time, that allows to set the dwell time on each point of the scan, determine the real definition of the image. Throughtout this map, we are able to align laser beams of pump and probe on the single nanoparticle.

Chapter 3

Experimental measurements

This chapter presents *pump & probe* measurements realized on gold nanospheres with a nominal diameter of 40 nm immobilized on a Sapphire layer (Al_2O_3). First, we describe nanoparticle's detection, that is the preliminary operation to perform the measure. Then, thermal and mechanical dynamics are discussed.

3.1 Overview

The aim of our work is the study and the analysis of termomechanical dynamics of a single nanoparticle. Sample's structure, realized throghout electronic litography, has been presented in section 2.3.2. We analyse two different samples:

- **No diluited Au**

  On this sample, pure gold nanospheres are immobilized on a 1 mg/ml concentration of antibody.

- **1:10 Au diluition**

  In this case, we have gold nanospheres in PBS solution, with a 1:10 diluition, immobilized on a 0.1 mg/ml concentration of antibody.

3.1.1 Single nanoparticle's detection

Exploiting the raster scan movement, we can create a map of our sample. Scanning on a nanosphere with a diameter of 40 nm, the ability to block the laser beam depends on its elec-

tromagnetic cross section σ, which is directly proportional to the nanoparticle's radius: $\sigma \propto R$. Therefore, the variation of voltage due to a scan on the Knife-edge is higher than the one due to the presence of a nanosphere. For this reason, it is important to have a waist as small as possible.

Detection and imaging have always been performed using the probe beam, which has a wavelenght of 780 nm. Every scan area on the sample is labelled by a dot and a Knife-edge, see Figure 3.1 (a), characterized by a letter and a number, that allow us to identify exactly the position of nanoparticles. First, we use a microscope with an high resolution to localize the cluster on the sample in which gold nanospheres are placed. Then, with the help of a CCD Camera, we can focalize the beam exactly on the identified area. At this point, we start looking for our spheres, knowing that, when the beam passes on a nanoparticle, we observe a small variation of transmitted power. As we shrink the scan area on a single nanoparticle, we obtain a clear image of the particle itself, ensuring that the beam is set exactly on the object we want to analyze. Examples of the image obtained through this kind of scan are shown in Figure 3.1.

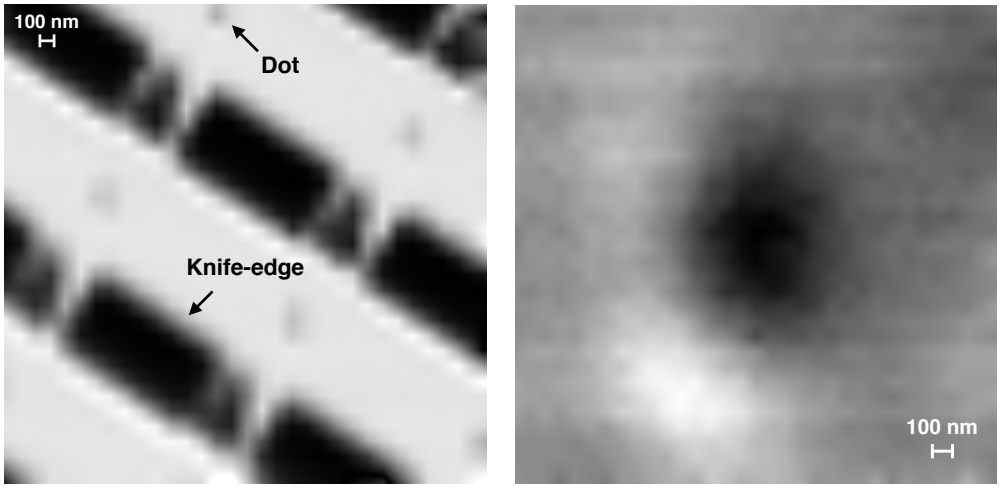

(a) Imaging of an area of the sample

(b) Probe beam's imaging through a single nanoparticle

Figure 3.1: Comparison between two imaging obtained scanning areas of different size. The scan area of (a) is 30000x30000 nm and shows the structure of the sample. Shrinking the scan area, (2000x2000 nm), we obtain a clear image of the single particle (b).

3.2 Time-resolved measurements on gold nanospheres

Once both *pump* & *probe* beams are well-positioned on the nanoparticle, we perform the time-resolved measurement with the ASOPS technique. The single pump pulse excites the particle, through the transfer of the absorbed energy δU. The absorbed energy produces first the heating of electrons, then their thermalization with particle's phonons. The effect is an increase of lattice's temperature from T to $T + \Delta T$, that causes a thermal expansion of the particle itself. As a result of electron's heating, there is a change in the dielectric electronic constant and a variation of nanoparticle's size, leading to an increase of the extinction cross section σ_{ext} of the sphere exposed to the probe beam. The increase of particle's temperature leads to an expansion and, then, to a decrease of beam's trasmitted power, according to Equation 2.8. As the cooling process takes place and σ_{ext} reaches the unperturbed value, the particle slowly returns to its thermomechanical equilibrium. This leads to a decrease of relative trasmittance $\Delta Tr/Tr$, that amounts to zero when the particle is completely thermalized with the substratum at temperature T. The variation of trasmitted power, ΔTr, is proportional to the voltage provided by the "RF-OUTPUT" channel of the differential photodetector, while the value of absolute trasmitted power, Tr, is proportional to the one measured by the "MONITOR+" channel. Because of the different conversion V/W of the two channels, there is an intrinsic conversion factor that has to be taken in account. As we are interested in the relaxation time of the sample, the exact value of the ratio is not significant, therefore an error due to this conversion factor can be neglected.

Analysis and curve fitting

The first step consists in acquiring the voltage produced by the probe beam, trasmitted through the sample, when the pump excites the particle. The value of ΔTr has been averaged on n temporal scans. Figure 3.2 shows a typical thermomechanical *pump & probe* measure. The value ΔTr provided by the photodetector has been divided by the voltage of probe's beam in absence of pump one, Tr, in order to obtain a relative variation.

We set a detuning frequency $\Delta\nu = 1KHz$ and the curve is normalized with respect to the maximum value. Observing the curve, we can identify the fast dynamic due to the electronic heating, with the characteristic time of the order of hundreds of femtoseconds. If we consider longer temporal scales, it is possible to recognize the two main events that we want to study:

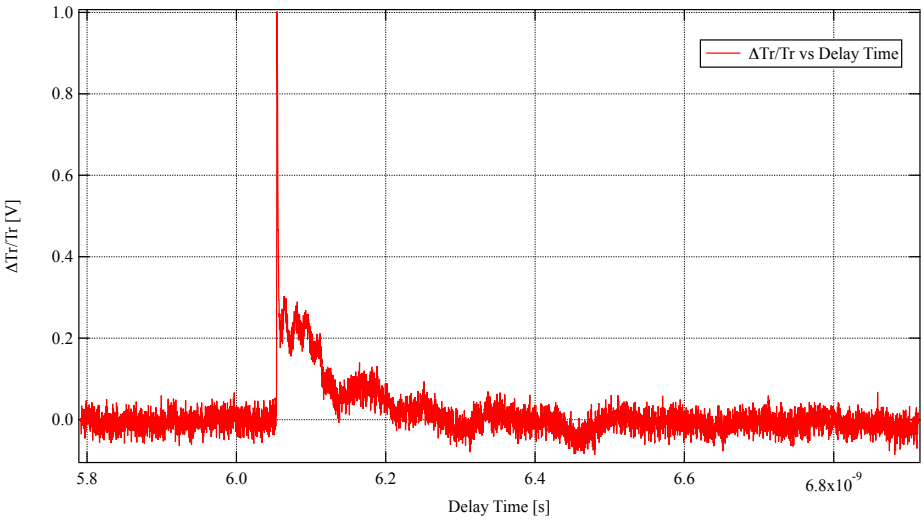

Figure 3.2: Relative variation of transmission versus time delay. The curve has been normalized with respect to the maximum value. Pump's power is 3 mW, probe's one is 200 μW. The detuning is set to $\Delta\nu = 1KHz$.

- The damping linked to the thermal relaxation between the nanoparticle and the substratum, in the order of hundred $ps - ns$.
- The mechanical nanoparticle's oscillation, showed in Figure 3.3, characterized by a period of about few ten ps.

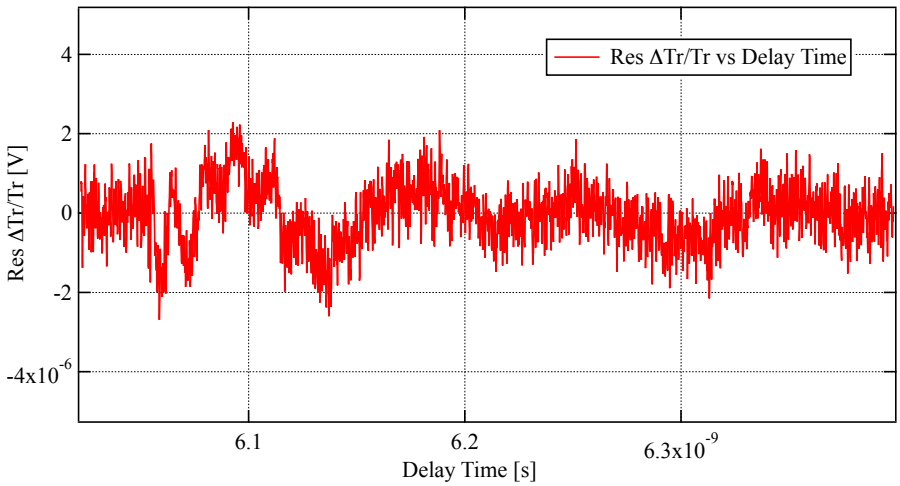

Figure 3.3: Residual of $\Delta Tr/Tr$ versus delay time obtained from the fit of curve in Figure 3.2.

3.3 Thermal analysis

We now analyze the thermal dynamics of the nanoparticle. Let us consider the rates of decay due to the heat flux between the nanoparticle and the substratum. To evaluate these temporal dynamics, we performed a fit on the experimental data, as shown in Figure 3.4.

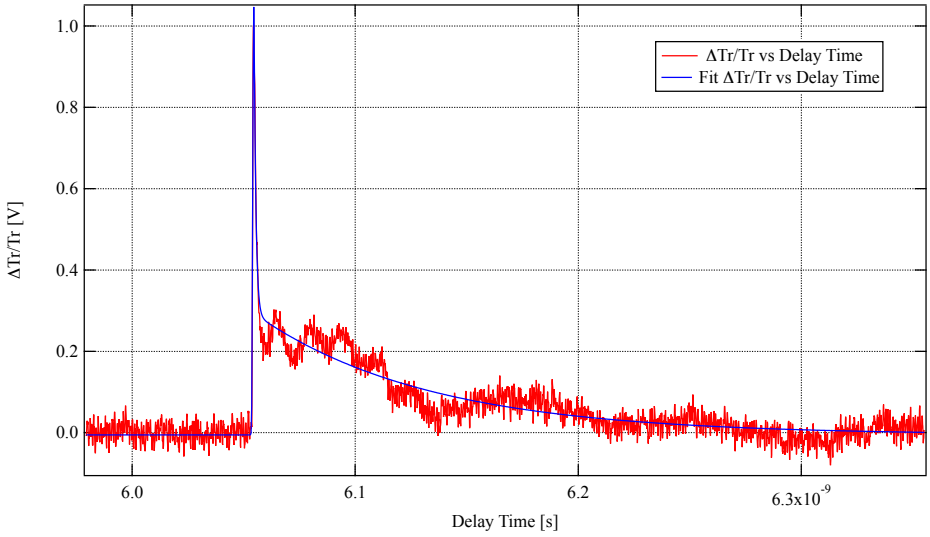

Figure 3.4: Red trace represents relative variation of trasmission, $\Delta Tr/Tr$, versus time delay. The curve has been normalized with respect to the maximum value. In blue, the fit function. The fit has been performed on the measure shown in Figure 3.2, with a pump's and probe's power of 3 mW and 200 μW, respectively. The detuning frequency is $\Delta\nu = 1KHz$.

The procedure used for the *curve fitting* is a linear combination of two exponentials and it is illustrated in Appendix A.1.

We are now interested in the analysis of fit coefficients, amplitude and rate of decay, one for each exponential, for both the sample with pure and 1:10 diluited gold nanoparticles, respectively related (with the corresponding confidence interval) in Table 3.1 and Table 3.2.

Through the analysis of these coefficients, we want to verify if the different diluition of the nanoparticles can in some way be a discriminating factor for our measurements, in other words if more or less high concentration of particle can influence the thermal temporal dynamics of the sample.

Plotting the rates of decay, τ_1 vs τ_2, as represented in Figure 3.5, we observe that there is only one representative time, which is typical of all the measures both for the pure and diluited nanoparticles, characterized by an ultrafast dynamic - of the order of hundreds of fs up to many

measure	τ_1 $[fs]$	τ_2 $[ps]$	A_1 $[V]$	A_2 $[V]$
02	816 (789, 843)	78 (77, 79)	0.1243 (0.1211, 0.1275)	0.0282 (0.0280, 0.0284)
10	1185 (1157, 1213)	75 (74, 76)	0.1124 (0.1105, 0.1143)	0.0219 (0.0217, 0.0221)
13	921 (895, 947)	67 (66, 68)	0.0929 (0.0909, 0.0949)	0.0303 (0.0301, 0.0305)
16	1463 (1448, 1478)	73 (72, 74)	0.0945 (0.0938, 0.0952)	0.0289 (0.0288, 0.0290)
18	1513 (1475, 1551)	76 (75, 77)	0.1115 (0.1045, 0.1185)	0.0242 (0.0240, 0.0244)
20	434 (393, 475)	72 (71, 73)	0.1352 (0.1236, 0.1468)	0.0472 (0.0470, 0.0474)

Table 3.1: Values of amplitude and rate of decay, one for each exponential, obtained from the fit of the measurements performed on the sample with no diluted nanoparticles. In round brackets, the corresponding confidence interval.

measure	τ_1 $[fs]$	τ_2 $[ps]$	A_1 $[V]$	A_2 $[V]$
21	732 (689, 775)	73 (71, 75)	0.1410 (0.1344, 0.1476)	0.0220 (0.0217, 0.0223)
23	824 (780, 868)	72 (71, 73)	0.1342 (0.1284, 0.1400)	0.0268 (0.0265, 0.0271)
29	906 (863, 949)	63 (61, 65)	0.1132 (0.1092, 0.1172)	0.0177 (0.1174, 0.0180)
30	523 (466, 580)	76 (74, 78)	0.1743 (0.1593, 0.1893)	0.0228 (0.0223, 0.0233)
31	765 (706, 824)	79 (76, 82)	0.1360 (0.1280, 0.1440)	0.0147 (0.0144, 0.0150)

Table 3.2: Values of amplitude and rate of decay, one for each exponential, obtained from the fit of the measurements performed on the sample with 1:10 diluited nanoparticles. In round brackets, the corresponding confidence interval.

ps - and a relaxation dynamic between particle and substratum of about 70 ps.

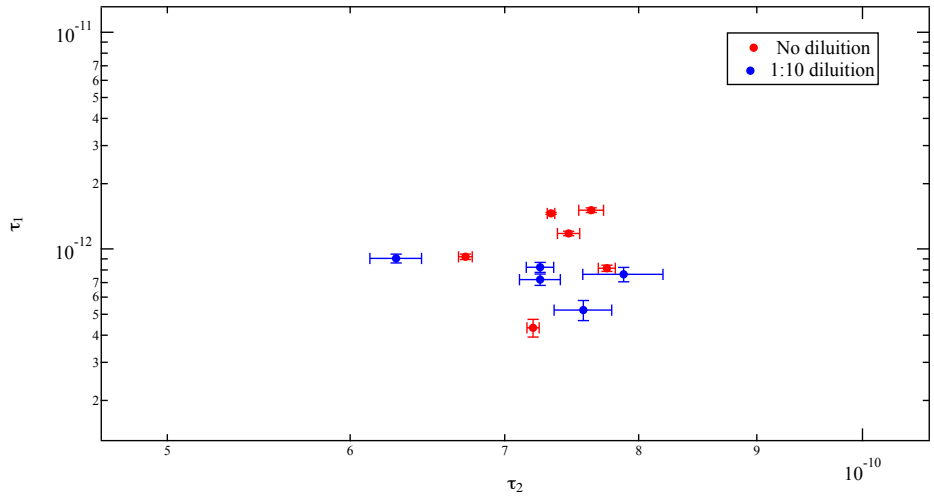

Figure 3.5: τ_1 vs τ_2 with the corresponding error bars, obtained from the fit on normalized curve. Red markers represent the values related to pure gold nanoparticles, while blue dots the ones linked to the sample with 1:10 diluition.

Subsequently, we show the amplitude of each exponential, A_1 versus A_2, as absolute value (Figure 3.6 (a)) or normalized value (Figure 3.6 (b)).

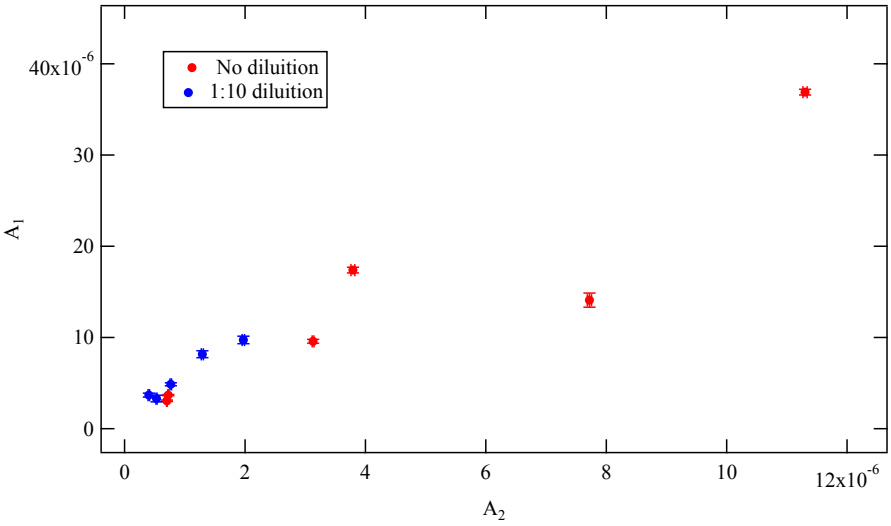

(a) Absolute values of A_1 *vs* A_2

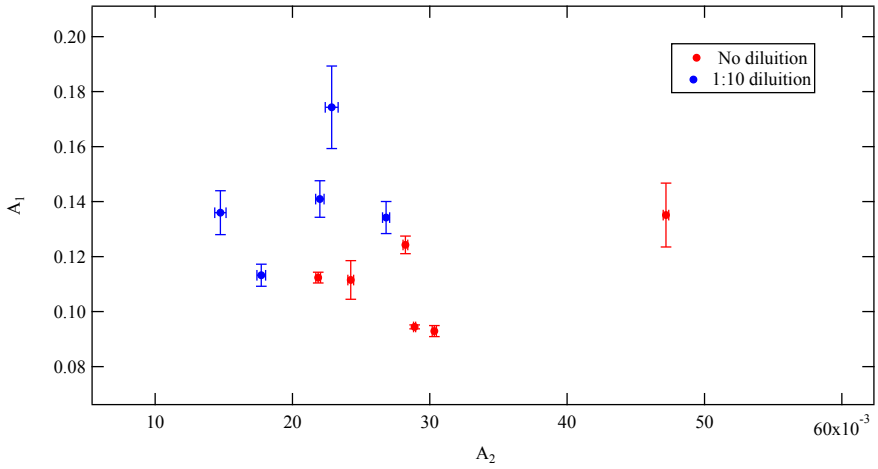

(b) Normalized values of A_1 *vs* A_2

Figure 3.6: A_1 vs A_2 with the corresponding error bars, obtained from the fit on absolute values (a) and normalized curve (b). Red markers represent the values related to pure gold nanoparticles, while blue dots the ones linked to the sample with 1:10 diluition.

Looking at the graphs, it is possible to see a clear difference in the arrangement of the points. In particular, it is interesting to observe that the trend to cluster around a certain value is more evident if we consider the normalized curve. These remarks point out that there is no real connection between the amplitude and rates of decay and the diluition of nanoparticles on the sample. A more detailed analysis could come from other methods as *cluster analysis* and data mining techniques.

As we can see, to each value of the parameter are associated the corresponding error bars, evaluated from the standard deviation of the measure itself. This uncertainty results from the process of statistical analysis followed by the programme. Indeed, while doing the fit, it estimates the *sum of squared errors* (SSE), which is the sum of the squares of the deviations of the actual values from the predicted ones. Once determined the value of each coefficient that minimize the deviations of the fit curve from the expected values, it evaluates the range of each parameter in which the fit remains appreciable, giving the corresponding confidence interval. This value is meaningful for the single measurement, but it has not a significant importance for the particular analysis that we want to perform, due to the fact that the dispersion of different values is wider than the error associated to the single measure. This divergence from the mean value, leading to a distribution of points around it, results from the so-called *systematic errors*, i.e., errors that are not determined by chance but are introduced by other variables inherent in the system. In general, this kind of error, linked to the reproducibility of experiments, is a component that remains constant or depends in a specific manner on some other quantity, for example temperature or humidity of the laboratory, variables that cannot be controlled.
For the purposes of our analysis it is interesting to note that the scatter of the points is much bigger than the error on the single measurement. We interpret this fact as the influences of external factors are more important than the single measurement's deviation.

3.4 Mechanical analysis

When an ultrashort pump pulse excites a metal particle, the absorbed energy is first conveyed to the conduction electrons, which collide within some tens of femtoseconds through electron-electron interactions. On a 1 *ps* timescale, the hot electrons thermalize with the lattice, and, still later, the whole particle cools down to ambient temperature via heat diffusion. The sudden heating of the electron gas has mechanical effects, as we can see in Figure 3.3. The vibrational properties of nano-objects have been extensively studied during the last decades because they offer many possibilities for their characterization (for instance to determine their size or cristallinity) and is a unique means for investigating their interaction with the environment.
The vibrational eigenmodes of a single material nano-object are usually described through a macroscopic model based on continuum mechanics and using bulk elastic constants of the con-

stituting materials. Although this approach disregards the discrete atomic structure of the objects themselves, it has been shown to excellently reproduce their vibrational frequencies and we will thus use it to describe the vibrations of gold nanospheres. We assume that our material is homogeneous and isotropic, i.e., polycrystalline, and we consider objects with spherical symmetry, that is formed by a spherical core of radius R_1, surrounded by m spherical shells of thickness $R_{j+1} - R_j$, and embedded in an infinite matrix, that constitutes the external environment.
We now consider a pure sphere (i.e., the m = 0 case), for which all normal modes can be computed semianalytically. However, as we are primarily interested in time-resolved investigations, we will only consider modes displaying radial simmetry, which are selectively launched in such experiments due to the isotropy of the excitation process. The displacement field associated with these modes, $\mathbf{u}(\mathbf{r}, t) = u(r, t)\mathbf{u_r}$, spatially depends only on the radial coordinate r, and it is the solution of the radial Navier equation

$$\rho \frac{d^2u}{dt^2} = (\lambda + 2\mu)\left[\frac{d^2u}{dr^2} + \frac{2}{r}\frac{du}{dr} - \frac{2u}{r^2}\right] \tag{3.1}$$

where λ and μ are the Lamè constants of the material forming the object, and ρ is its density. The eigenmodes correspond to harmonic solutions of Equation 3.1:

$$u(r, t) = u(r) \exp(i\tilde{\omega}t) \tag{3.2}$$

where the vibrational frequencies $\tilde{\omega}$ are real or complex valued in the case of free and matrix-embedded particles, respectively. In the latter case, their imaginary part reflects damping of the vibration mode by the transfer of mechanical energy to the matrix. As for the vibration of a macroscopic resonator, the properties of vibrational eigenmodes, i.e., their frequency $\tilde{\omega}$ and displacement field $u(r)$, are thus imposed by the boundary conditions, that is continuity of the displacement and of the radial component of the stress tensor σ_{rr} at the nanoparticle-matrix interface. For a radial mode, σ_{rr} is connected to the field $u(r, t)$ by

$$\sigma_{rr} = (\lambda + 2\mu)\frac{du}{dr} + 2\lambda\frac{u}{r} \tag{3.3}$$

Assuming that the sphere is not embedded in any matrix (Figure 3.7) the boundary condition

is given by

$$\sigma_{rr}(R) \;=\; 0 \tag{3.4}$$

where R stands for the particle's radius.

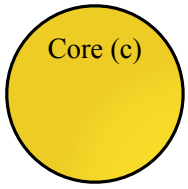

Figure 3.7: Example of a free pure gold nanosphere.

Eigenfrequencies are given by

$$\xi \cot \xi = 1 - \frac{\xi^2}{4}\left(\frac{C_L}{C_T}\right)^2 \qquad \text{with} \quad \xi = \frac{\omega R}{C_T} \tag{3.5}$$

In Equation 3.5, C_L and C_T stand for longitudinal and trasversal velocity of sound in the specific material[1], respectively.

If we suppose that the nanoparticle is embedded in an infinite matrix, as schematically shown in Figure 3.8, the Navier equation becomes

$$\xi \cot \xi = 1 - \frac{\xi^2(1 + i\xi/\alpha)}{\eta\xi^2 - 4\alpha^2\gamma^2(1 - 1/\eta\beta^2)(1 + i\xi/\alpha)} \tag{3.6}$$

with

$$\alpha = C_L^{(m)}/C_L^{(c)}, \qquad \beta = C_T^{(m)}/C_T^{(c)}, \qquad \gamma = C_T^{(m)}/C_L^{(m)}, \qquad \eta = \rho^{(m)}/\rho^{(c)}$$

Evaluating the effect of the external environment, there are two boundary conditions: first, the continuity of displacement and stress, in addition the diverging acoustic wave in the matrix. This model is generalizable to an arbitrary number of layers and gives a solution similar to Equation 3.2, with complex $\tilde{\omega}$, i.e., complex frequencies that imply energy dissipation. The second result is a weak modification of vibration frequencies, that become lower because of the

[1]For the value of constants, see [20]

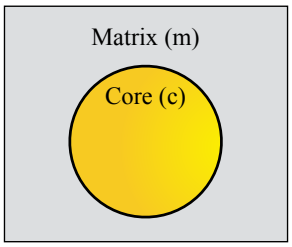

Figure 3.8: Gold nanosphere embedded in a matrix.

presence of a matrix around the particle. In this case, the eigenmodes of the nanoparticle are no longer exactly eigenmodes, but *quasi-steady states*, that is particle's modes subject to a damping.

To find the frequencies of particle's mechanical oscillations, we compute a *Discrete Fourier Transform* (DFT) of the residual between signal measured and the double-exponential fit performed. The DFT relates the function's time domain to the function's frequency domain and it is defined conventionally as

$$\hat{f}(\mathbf{k}) = \int_{-\infty}^{+\infty} f(\mathbf{x}) e^{-2\pi i \mathbf{k}\cdot\mathbf{x}} d\mathbf{x} \tag{3.7}$$

$$\hat{f}(\mathbf{x}) = \int_{-\infty}^{+\infty} f(\mathbf{k}) e^{2\pi i \mathbf{k}\cdot\mathbf{x}} d\mathbf{k} \tag{3.8}$$

Equations 3.7 and 3.8 are equivalent to the *Fast Fourier Transform* (FFT), that computes the discrete summation

$$F_k = \sum_{n=1}^{N} f_n e^{-2\pi i (k-1)(n-1)/N}, \quad 1 \leq k \leq N \tag{3.9}$$

with F_k the DFT of a signal f_n (with index $n = 1, 2, \ldots, N$). The inverse transform is given by

$$f_n = \frac{1}{N} \sum_{n=1}^{N} F_k e^{-2\pi i (k-1)(n-1)/N}, \quad 1 \leq k \leq N \tag{3.10}$$

Our signal is formed by a discrete number of points N, so the best frequency resolution of FFT is

$$\Delta\nu_{FFT} = \frac{1}{N \cdot \Delta t} = \frac{1}{t_{max}} \tag{3.11}$$

where Δt and t_{max} are the resolution and the temporal window of the measure, respectively.

An example of the residual and the relative *Power spectrum* is shown in Figure 3.9

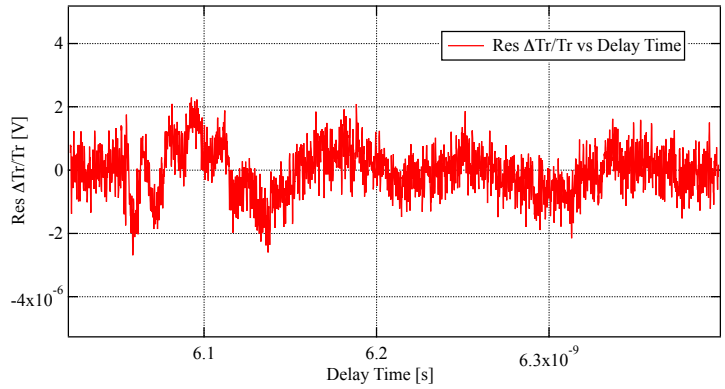

(a) Residual $\Delta Tr/Tr$

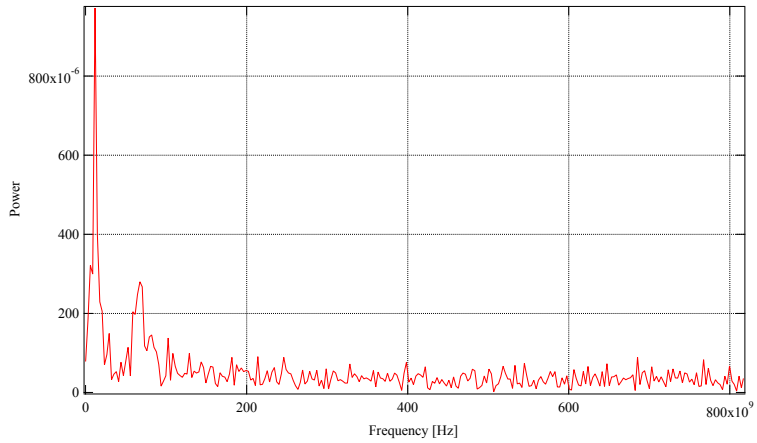

(b) Power spectrum

Figure 3.9: (a) shows the residual of $\Delta Tr/Tr$ versus delay time obtained from the fit represented in Figure 3.4. In (b) we can see the Power Spectrum of residual in (a). It is interesting to observe two peaks, corresponding to the frequencies of the two oscillations evident in (a).

From the values of frequencies, it is possible to estimate the period of these mechanical oscillation as the inverse of frequency itself: $T = \frac{1}{\nu}$. Looking at the residual of $\Delta Tr/Tr$ (Figure 3.3), we can see that there is a damping of the mechanical oscillations. We are now interested in finding and analysing the rates of decay. To do this, we have performed a fit of the experimental data, as shown in Figure 3.10, using a linear combination of two damped sines[2].

As for the thermal analysis, we are interested in fit coefficients, amplitude A, angular frequency ω and phase ϕ, for each oscillators of both samples. First of all, we want to examine if

[2]For the complete procedure, see Appendix A.2

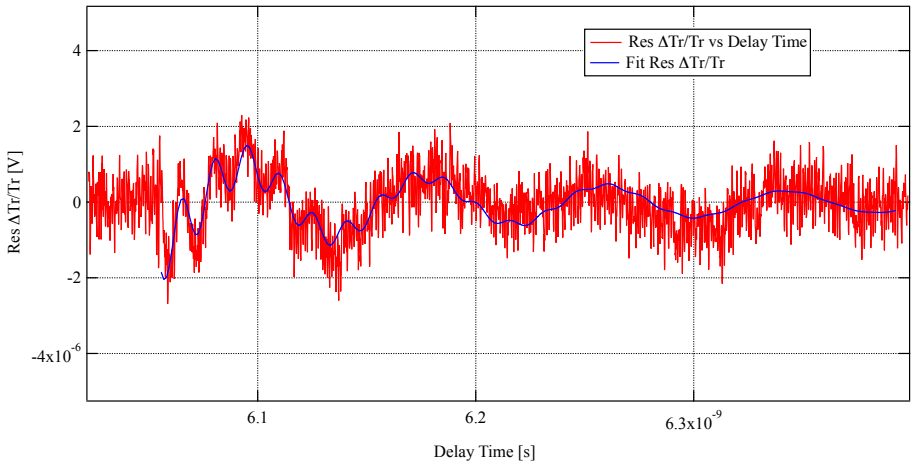

Figure 3.10: Residual of $\Delta Tr/Tr$ (red trace) and fit curve obtained with two damped sines (blue trace).

there is any trend to cluster. To do this, we plot each fit coefficient for the first oscillator versus the corresponding value for the second one. The results are represented in Figure 3.11.

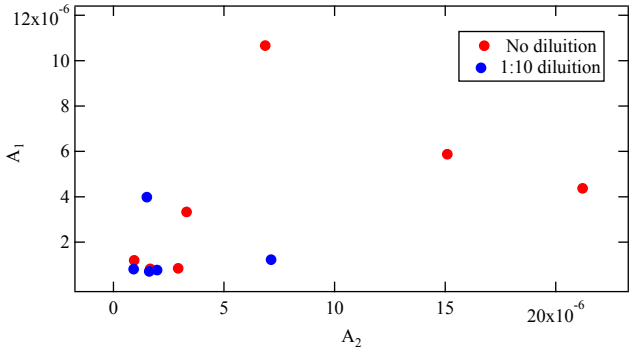

(a) A_1 *vs* A_2

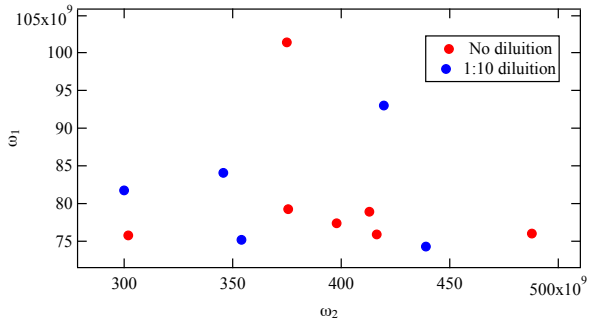

(b) ω_1 *vs* ω_2

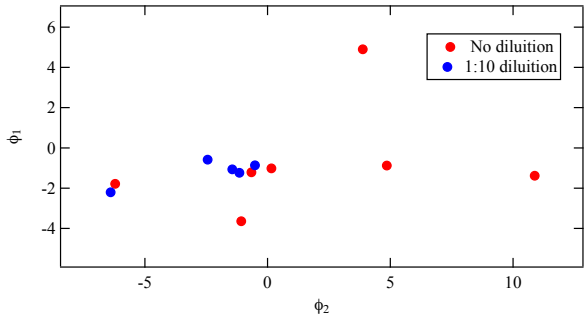

(c) ϕ_1 *vs* ϕ_2

Figure 3.11: Amplitude A, angular frequency ω and phase ϕ for the first oscillator versus same coefficients for the second one. Red markers represent the values corresponding to the sample with pure gold nanoparticles, while blue dots the ones corresponding to the sample with 1:10 diluited nanospheres.

Looking at the graphs, we can deduce that it is not possible to identify a real trend to cluster,

therefore such a kind of analysis does not allow us to distinguish one sample from the other, that is the different diluition of nanoparticles on the substratum does not affect significantly the evaluated mechanical fit coefficients. However, it is important to remind that the scatter of the points, which is much more important than the deviation of a single measurement, is due to external factors here neglected. Though, it is interesting to find the theoretical eigenfrequencies of the particle's radial eigenmodes and compare them with the values obtained from the fit. Along these lines, we will proceed in two ways:

- We suppose to fix the value of our particle's radius at $20nm$ and we observe the position of period vs radius with respect to the theoretical eigenfrequencies obtained by solving the Navier equation.
- Projecting the value of the period obtained experimentally on the line of theoretical eigenfrequencies, we find the radius of the nanoparticle.

The first step of the analysis consists in finding the values of eigenfrequencies, solving Equation 3.5, that is finding the intersection points of $\xi \cot \xi$ and the parabola $\frac{\xi^2}{4}\left(\frac{C_L}{C_T}\right)^2$. Once found the value of ξ, knowing that $\omega = 2\pi\nu$, eigenfrequencies are calculated as

$$\nu = \frac{\xi \cdot C_L}{2\pi R} \tag{3.12}$$

The problem can be solved both graphically, plotting in the same plane the two functions and acquiring the intersection points, and algebraically, through mathematics programs. The graphic solution in represented in Figure 3.12.

The values of ξ, corresponding to the fundamental breathing mode and to the first eigenmodes, $n = 0$ and $n = 1$ respectively, are

$$\xi_0 = 2.94528 \qquad \text{for} \qquad n = 0 \tag{3.13}$$

$$\xi_1 = 6.19355 \qquad \text{for} \qquad n = 1 \tag{3.14}$$

From these values, we obtained the corresponding eigenfrequencies for different radius of the particle, from 5 nm to 50 nm, that are related in the following Table.

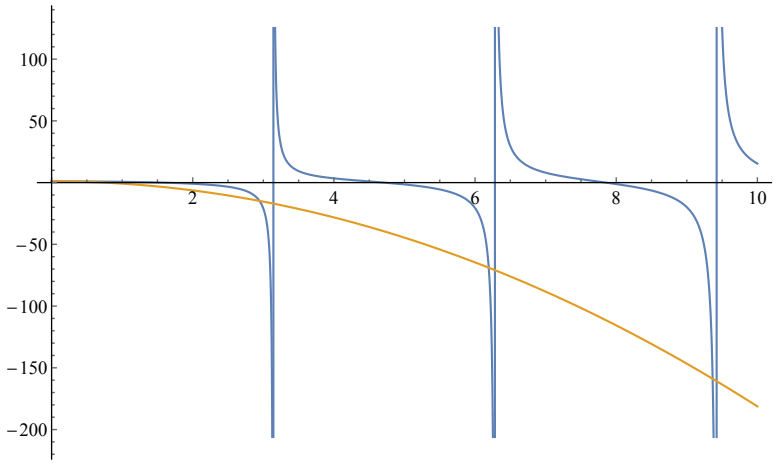

Figure 3.12: Graphical representation of functions $\xi \cot \xi$ (blue trace) and $1 - \frac{\xi^2}{4}\left(\frac{C_L}{C_T}\right)^2$ (yellow line). The values of ξ are given by the intersection points.

R [nm]	$\nu_0(R)$ $[GHz]$	$\nu_1(R)$ $[GHz]$	ν_{COMSOL} $[GHz]$
5	303.8	639	326
10	151.9	319.4	163
15	101.3	212.9	109
20	75.9	159.7	82
25	60.8	127.8	65
30	50.6	106.5	54
35	43.4	91.3	47
40	38.0	79.8	41
45	33.8	71.0	36
50	30.4	63.9	33

Table 3.3: Values of eigenfrequencies for the fundamental and second breathing mode, ν_0 and ν_1 respectively, and theoretical values obtained from a simulation with COMSOL, ν_{COMSOL}. All the frequencies have been calculating for different values of the radius, from 5 to 50 nm.

The last column, ν_{COMSOL}, represents the values of frequency with radius variations provided by COMSOL Multiphysics, a specific simulator software, for the fundamental breathing mode ($n = 0$). In Figure 3.13 and Figure 3.14 are shown the two-dimensional and three-dimensional graphic simulations, respectively, of the fundamental breathing mode of a gold nanosphere with a radius of 25 nm.

Looking at the table, we can observe that values provided by the software are slightly higher than those gained from the solution of Navier equation and frequency linked to the first eigenmode, $n = 1$, is about two times the frequency corresponding to $n = 0$. It is important to remind that we are able to excite, that is to see, only eigenmodes with the same symmetry of

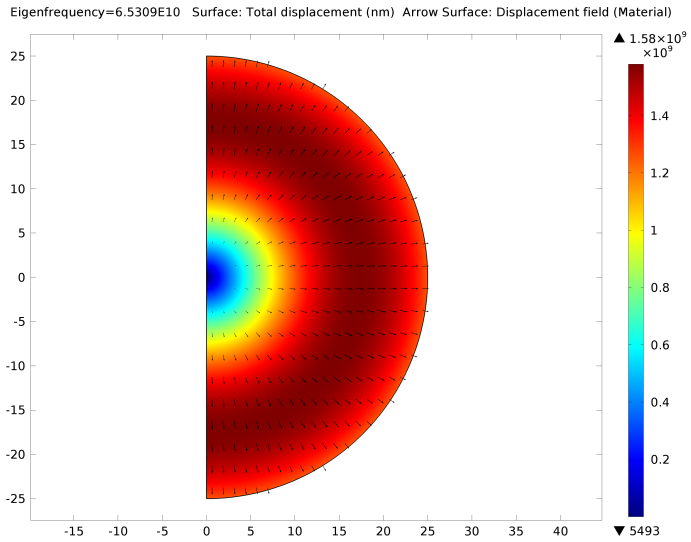

Figure 3.13: Two-dimensional simulation of the fundamental breathing mode of a gold nanosphere with a radius of 25 nm. The blue area represents the nodal point of the eigenmode, that is the area of sphere which is not subjected to any displacement. As we can see, for this specific breathing mode, there is only one nodal point located in the centre of the particle. In red are represented the areas of maximum expansion. Black arrows show the direction and the intensity of the displacement.

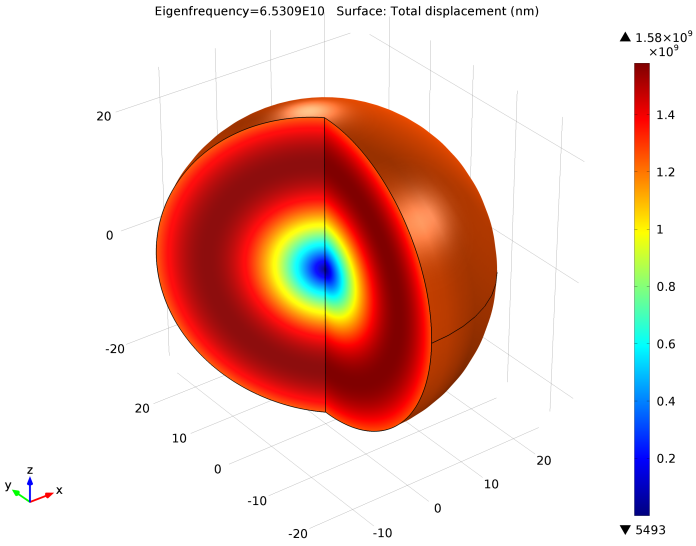

Figure 3.14: Three-dimensional simulation of the fundamental breathing mode of a gold nanosphere with a radius of 25 nm. In blue is shown the nodal point of the displacement, while in red are represented the areas of maximum expansion.

the particle's starting displacement. Knowing that the relation between period of oscillations and particle's size is given by

$$T_{osc} \approx \frac{D}{C_L}, \quad \text{where} \quad D = 2R \tag{3.15}$$

we can plot the inverse of ν, i.e., the period T, for each different excited eigenmodes, versus radius R, and verify their direct proportionality.

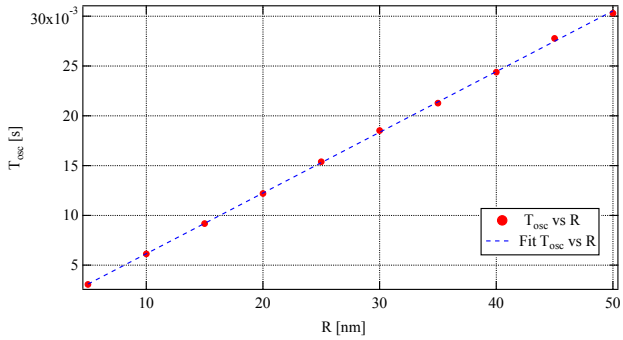

(a) T_{Comsol} *vs* R

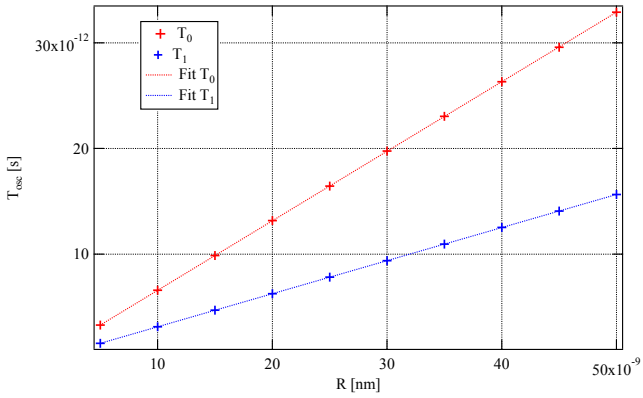

(b) T_{osc} *vs* R

Figure 3.15: Linear dependence of period on the size of the particle shows for the theoretical values obtained from COMSOL, (a), and for the ones acquired from the solution of Navier equation, (b).

The fit function used is a line, defined as $y = a + bx$, where a stands for the y-intercept of the line and it is 0 in this case, while b, the slope of the line, assumes two different values, corresponding to $n = 0$ and $n = 1$ modes. The first analysis consists in plotting the oscillation periods obtained from the fit of experimental data versus $R = 20nm$, which is the value of particle's radius given by the datasheet. In this way, we can observe if there is any particular distribution around the expected value of period. In doing this analysis we divided the experimental periods of pure nanoparticles from the ones of diluited nanoparticles, and the results are shown in Figure 3.16 and Figure 3.17, respectively.

Observing Figure 3.16, we can recognize two different cluster of points, green ones and black ones. The former, representing a period of $\sim$ 15 ps, is similar to the theoretic value corre-

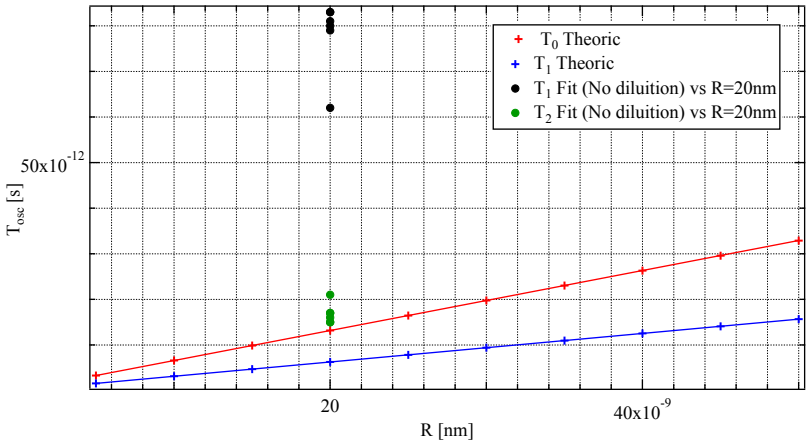

Figure 3.16: First (black markers) and second (green markers) oscillation periods obtained from the fit of experimental measures performed on pure nanoparticles versus nominal value of radius provided by the constructor, R=20 nm.

sponding to the fundamental breathing mode ($n = 0$) calculated for a free gold nanosphere. Although the experimental values are slightly higher than the theoretical one, we can infer that they are confident, due to the fact that the presence of an external environment, neglected in the evaluation of theoretical period, reduces the frequency of oscillations, leading to an increase of the period. As we can see, the second group of points, identified by black markers, is far from both the theoretic lines that represent the fundamental and the first radial breathing mode of a sphere. In this case, we have oscillation periods of $\sim$ 80ps (corresponding to values of frequencies of the order of $\sim$10 GHz), higher than the ones ascribed to the eigenmodes of a gold nanosphere, between 5 and 15 ps. Those values could be associated to the oscillations of the streptavidin-biotin antibodies system, characterized by an high affinity. The possibility to observe the period, i.e., the frequency, of the biological system that characterized our sample is extremely interesting and it would be of primary importance in order to distinguish the different structure of the particular biological composition connected to the nanoparticle.

Figure 3.17 shows the measurements on the sample with diluited nanoparticles. The distribution of periods is similar to the one seen for the first sample, with a group of points focused around the expected value for the fundamental breathing mode of a free sphere, and the other one characterized by a period of $\sim 80ps$, far from values typical of the first eigenmode. This fact allows us to reach an important conclusion, that is different diluition of nanoparticles has not a significant effect on the mechanical oscillations that we are interested to analyze. Moreover, we

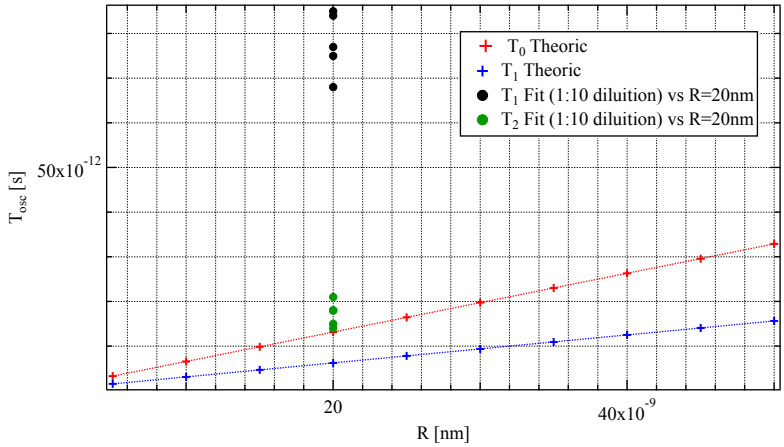

Figure 3.17: First (black markers) and second (green markers) oscillation periods obtained from the fit of experimental measures performed on 1:10 diluited nanoparticles versus nominal value of radius provided by the constructor, R=20 nm.

can suppose that all our measurements have been always performed on a single nanoparticle, due to the direct proportionality between period of oscillations and size of particles.

At this stage, there is another kind of analysis that we can perform, that allows us to find the distribution of nanoparticle's radius around the value of 20 nm provided by the constructor. To do this, we got the value of the slope of both lines, b_0 and b_1, from the fit, then we solve the inverse equation

$$R = \frac{T}{b} \tag{3.16}$$

From the results previously obtained and discussed, we can expect that this evaluation is reasonable only for the period of sphere's oscillations and that it gives believable results if those oscillations are related to the fundamental breathing mode. For this reason we have considered T_2, that is $\sim 15ps$, and calculated the corresponding value of radius. Results are represented in the following graphs.

Figure 3.18 shows the oscillation period of the nanospheres on the sample with no diluited particles versus the value of radius obtained by solving the equation $T_0 = b_0 R$. It is interesting to observe that the range of values is between 20 and 35 nm, i.e., the diameter of particles is about $40 - 70$ nm. Knowing that the mean diameter provided by the constructor is 20 nm, we can suppose that all our measurements have been performed on a single nanoparticle, leading

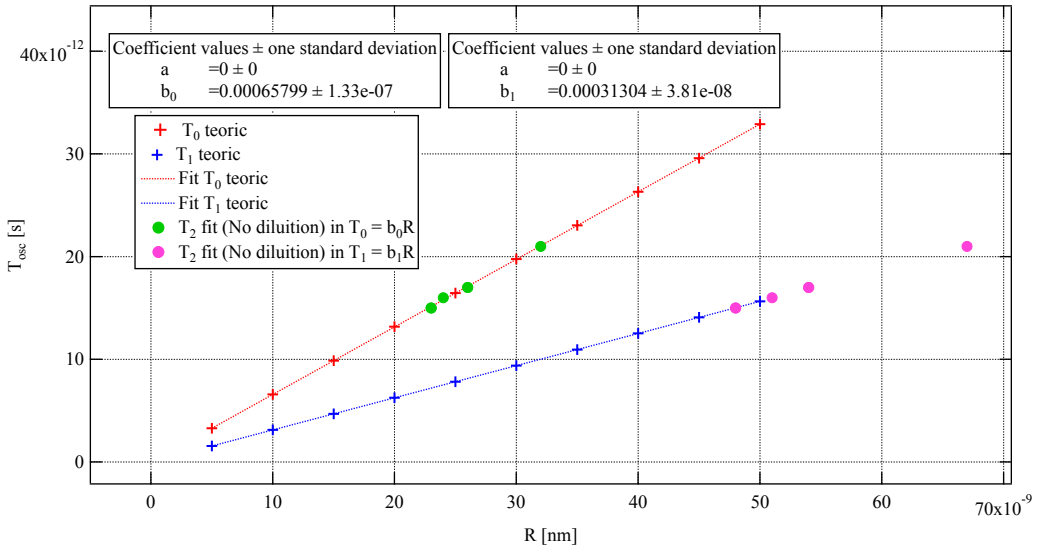

Figure 3.18: Distribution of particles' radius for pure gold nanospheres in the case of excitation of fundamental breathing mode (green markers) or when the first eigenmode of a sphere is excited (violet markers). Only the shorter experimental oscillation period T_2 has been considered.

to excite and, then, observe the fundamental breathing mode of a gold sphere.

By contrast, pink markers represent the period versus the value of radius provided by equation $T_1 = b_1 R$, giving higher size of particle, which would have a diameter of about $90 - 140\ nm$. These results are not confident with the expected value, proving that we are not observing the first eigenmode of the sphere.

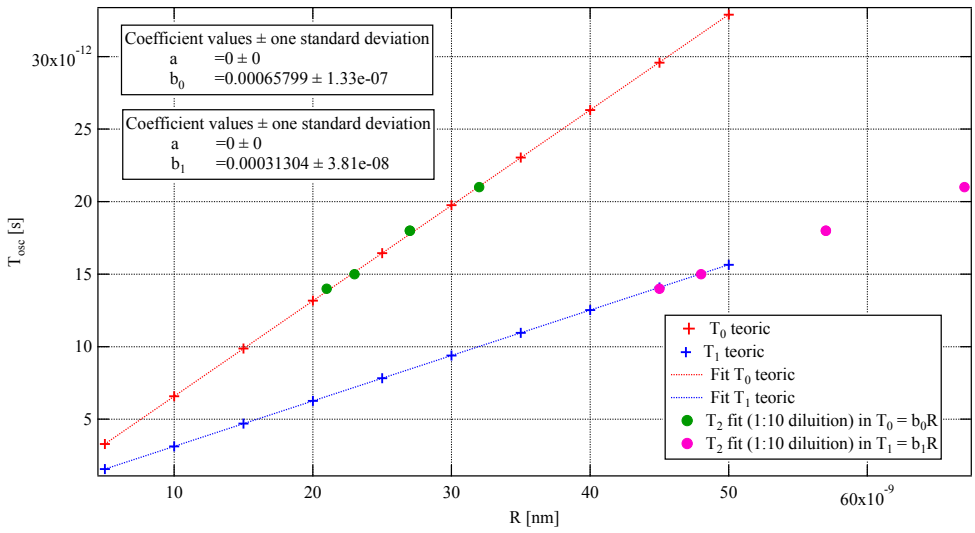

Figure 3.19: Distribution of particles' radius for 1:10 diluited gold nanospheres in the case of excitation of fundamental breathing mode (green markers) or when the first eigenmode of a sphere is excited (violet markers). Only the shorter experimental oscillation period T_2 has been considered.

Figure 3.19 represents the results obtained by performing the same analysis on the sample with diluited gold nanoparticle. It is important to underline the same distribution of the size of particles, that justify and confirm the hypothesis of evaluating the fundamental eigenmode of a single nanosphere.

Chapter 4

Conclusions and future perspectives

The aim of this thesis is to analyze and study optical properties of gold nanoparticles immobilized on a functionalized surface through the strong chemical bond between biotin and streptavidin. To do this we performed *pump & probe* measurements on samples with two different diluitions of nanospheres and compared the results in order to evaluate if there is any connection between the concentration of nanoparticles and their thermomechanical dynamics, that allows to distinguish the different composition of the samples.

Our work has been developed in two ways: first, we studied the thermal dynamics of nanoparticles, then we focused on the analysis of mechanical oscillations, trying to find and understand their nature.

From the evaluation of thermal properties we obtain informations about amplitude and rate of decay of exponentials, that allow us to observe the presence of a single characteristic time, linked to the thermal dynamics, independent from the concentration of particles, but an early trend of amplitudes to cluster around a mean value, slightly different depending on the diluition of the sample. This informations can be improved further, making a more detailed analysis, such as *cluster analysis*, in order to provide a more accurate picture on the actual trend to cluster.

Afterwards, the study of mechanical dynamics has been presented, obtaining the oscillation periods and the corresponding relaxation times. Doing an analysis similar to that carried on the thermal part, we are not able to find any meaningful distinction between the different samples. However, it is interesting the comparison between the frequencies obtained from the experimental data and the theoretical values given by the eigenfrequencies of the corresponding excited eigenmodes. From the dependence of oscillation period on the size of particles, supposing to

know the exact value of particle's radius, we can observe a significant trend to cluster around the corresponding value of eigenfrequency for the fundamental breathing mode of a sphere, that underline the excitation of the mode itself. By contrast, assuming that the right size of particles is unknown and that the excited eigenmode is the fundamental one, we observe a reasonable distribution of radius around the nominal value provided by the constructor.

Although these analysis allow us to make interesting considerations, there are some aspects that can be improved in the future. First of all, it would be interesting to evaluate the influence of the external environment on the oscillation period of sphere, estimating the theoretical eigenfrequencies for a matrix-embedded particle. Then, it would be important to understand if there is any connection between the oscillation of the biotin-streptavidin bond, that immobilized gold nanoparticles on the surface, and the low-frequency oscillation experimentally observed.

Appendix A

Fit procedures

In this Appendix we show the complete fit functions used both for the thermal and mechanical analysis, explaining the meaning of coefficients.

A.1 Thermal fit

For the thermal analysis, the fit function is a linear combination of two exponentials, expressed by the following equation

$$f(x) = x \cdot \left[A_1 \exp\left(-\frac{x}{|\tau_1|} \right) + A_2 \exp\left(-\frac{x}{|\tau_2|} \right) \right] \tag{A.1}$$

In Equation A.1, A represents the amplitude of each exponential and τ is the rate of decay. In our analysis we imposed the condition $x \geq 0$.

A.2 Mechanical fit

The function used for the fit of mechanical oscillations is a sum of two damped sines and it is given by

$$\begin{aligned} f(x) = \hat{x} \cdot \left\{ \sin\left[\omega_1 (x - x_0) + \phi_1 \right] \right\} \cdot x \cdot A_1 \exp\left[-\frac{x - x_0}{\tau_1} \right] \\ + \ \left\{ \sin\left[\omega_2 (x - x_0) + \phi_2 \right] \right\} \cdot x \cdot A_2 \exp\left[-\frac{x - x_0}{\tau_2} \right] \end{aligned} \tag{A.2}$$

where ω is the angular frequency of oscillations, ϕ is the phase, A represents the amplitude of exponential and τ the corresponding rate of decay. x_0 is the value on the x-axis where the fit starts and we impose two conditions on $\hat{x}$ and x, rexpectively: $\hat{x} \geq x_0$ and $x \geq 0$.

Appendix B

Electronics and devices

B.1 High-speed Photodetector

Let's describe the characteristics of electronic devices used for data acquisition. The Balanced Amplified Photodetector Thorlabs PDB430A is characterized by two channels, reason why we define it as *differential photodetector*. Both the ASOPS system and the technique adopted require this kind of detector in order to acquire the signal difference between the intensity of the transmitted and the reference beam. The technical specifications of these devices satisfy the needed requirements. In particular, we need an high temporal resolution and a low noise.

B.1.1 Differential Photodetector: PDB430A

Thorlabs PDB4xx series Balanced Amplified Photodetectors consist of two well-matched photodiodes and an ultra-low noise, high-speed transimpendance amplifier that generates an output voltage (RF OUTPUT) proportional to the difference between the photocurrents in the two photodiodes, i.e. the two optical input signals. Additionally, the unit has two monitor outputs (MONITOR+ and MONITOR-) to observe the optical input power levels on each photodiode separately.

Figure B.1 shows a functional block diagram of the PDB4xx series balanced amplified photodetectors.

The PDB4xx series is powered by external power supply ($\pm 12\ V$, $200\ mA$). The main features of photodetector are related in Tables B.1 and B.2. Table B.1 lists common technical data of the PDB4xx series, while Table B.2 lists the individual features of Thorlabs PDB430A. To avoid

damaging the photodiodes, it is important to monitor beams' intensity.

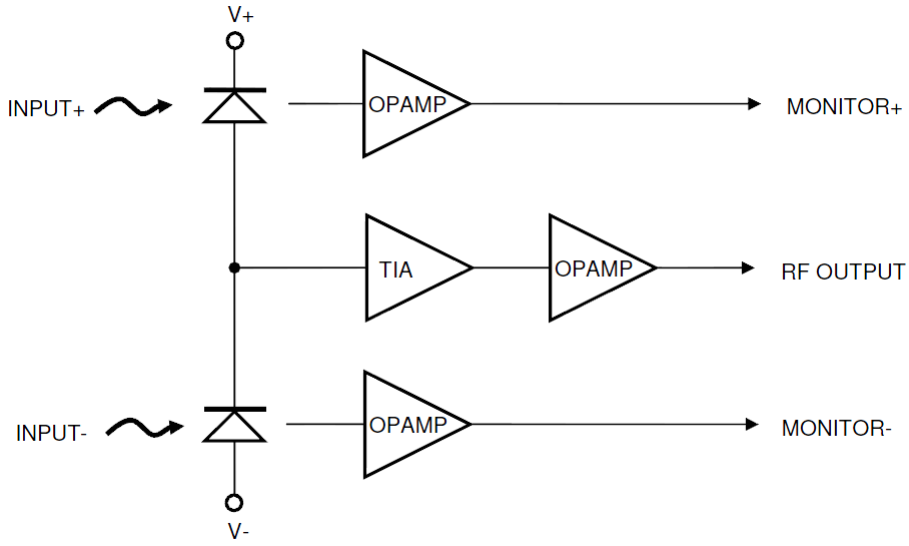

Figure B.1: PDB4xx Series Functional block diagram

Common Technical Data - PDB4xx Series	
Max. Input Power	20 mW (photodiode damage threshold)
RF-Output Impendance	50 Ω
RF OUTPUT voltage swing, max.	± 3.6 V (high impendance load)
Monitor Output Impendance	220 Ω
Monitor Output Bandwidth	DC 1 MHz
Conversion Gain Monitor Outputs	10 V/mW @ peak responsivity
Monitor Output voltage noise	180 μV RMS
DC-offset MONITOR Outputs	$<$ ± 2 mV
Size	85x80x30 mm^3
Power Supply	± 12 V, 200 mA

Table B.1: Common features of PDB4xx Series. All technical data are given at 23 ± 5 °C and 35 ± 15% relative humidity.

Individual Technical Data - Thorlabs PDB430A	
Detector Material/Type	Si / PIN
Wavelenght Range	320 nm - 1000 nm
Typical Max. Responsivity	0.5 A/W
Detector Diameter	0.4 mm
RF-Output Bandwidth (3dB)	DC - 350 MHz
Transimpendance Gain	10 x 103 V/A
Conversion Gain RF-Output	$5x10^3$ V/W
CW Saturation Power	720 μW @ 820 nm
Overall output voltage noise	1.5 mV RMS

Table B.2: Individual features of Thorlabs PDB430A

Appendix C

Acronyms

ASOPS	*ASynchronous Optical Sampling*
ECOPS	*Electrically Controlled OPtical Sampling*
CCD	*Charge-Coupled Device*
HR	*High Reflectivity*
PBS	*Phosphate Buffered Saline*
SPM	*Scanning Probe Microscopy*
DFT	*Discrete Fourier Transform*
FFT	*Fast Fourier Transform*
SSE	*Sum of Squared Errors*
C_L	*longitudinal velocity of sound*
C_T	*transversal velocity of sound*
δU	*energy density*
$\Delta\nu$	*detuning frequency*
T_{osc}	*oscillation period*
T	*temperature*
P	*power*
A	*amplitude*
I	*intensity*
R	*radius of the particle*
D	*diameter of the particle*
σ_{ext}	*effective cross section*

σ_{rr} *stress tensor*

u_r *displacement field*

ν *frequency*

f *focal lenght*

λ *wave length*

τ *rate of decay*

ρ *mass density*

ω *angular frequency*

ϕ *phase*

Bibliography

[1] G. Chen *Nanoscale energy transport and conversion*, Oxford University Press, 2005

[2] O.V. Salata *Applications of nanoparticles in biology and medicine*, Journal of Nanobiotechnology, 2004, **2**: 3

[3] S.E. McNeil *Nanotechnology for the biologist*, J. Leukoc. Biol., 2005, **78**: 585-594

[4] M. Bruchez, M. Moronne, P. Gin, S. Weiss, A.P. Alivisatos *Semiconductor nanocrystals as fluorescent biological labels*, Science, 1998, **281**: 2013-2016

[5] A. Bhirde, J. Xie, M. Swierczewska and X. Chen *Nanoparticles for cell labelling*, Nanoscale, 2011, **3**: 142-153

[6] K. Cho, X. Wang, S. Nie, Z. Chen and D.M. Shin *Therapeutic Nanoparticles fro Drug Delivery in Cancer*, Clin. Cancer Res, March 1, 2008, **14**; 1310

[7] S.J. Douglas, S.S. Davis, L. Illum *Nanoparticles in Drug Delivery*, Critical Reviews in Therapeutic Drug Carrier Systems, 1987, **3(3)**: 233-261

[8] S. R. Dave and X. Gao *Monodisperse magnetic nanoparticles for biodetection, imaging and drug delivery: a versatile and evolving technology*, Nanomed. Nanobiotechnol., 2009, **1**: 583-609

[9] E.S. Day, J.G. Morton, J.L. West *Nanoparticles for Thermal Cancer Therapy*, Journal of Biomechanical Engineering, July 2009, Vol. 131/074001-5

[10] L. Sola, M. Chiari (2012) *J. Chromatogr. A*, **1270**: 324-329

[11] F. Medeghini (A.A. 2013-2014) *Temporal characterization of short laser pulses in microscopy*, Tesi di Laurea Magistrale in Fisica, Università Cattolica del Sacro Cuore, Brescia

[12] A. Sterzi (A.A. 2011-2012) *Time resolved microscopy on nanostructured materials*, Tesi di Laurea Magistrale in Fisica, Università Cattolica del Sacro Cuore, Brescia

[13] S. Peli (A.A. 2009-2010) *Progetto e realizzazione di un apparato per spettroscopia ottica risolta in tempo mediante onda evanescente*, Tesi di Laurea Magistrale in Fisica, Università Cattolica del Sacro Cuore, Brescia

[14] Menlo System (April 15, 2009) *ASOPS White Paper*

[15] A. Canteri (A.A. 2010-2011) *Studio di fattibilità di una microscopia ottica risolta in tempo basata su tecnica ASOPS*, Tesi di Laurea in Fisica, Università Cattolica del Sacro Cuore, Brescia

[16] X. Luo, A. Morrin, A.J. Killard, M.R. Smyth (October 17, 2005) *Application of Nanoparticles in Electrochemical Sensors and Biosensors*, School of Chemical Sciences, National Centre for Sensor Research, Dublin City University, Dublin 9, Ireland

[17] A. Ronchi (A.A. 2012-2013) *Termomeccanica impulsiva di un singolo nanodisco*, Tesi di Laurea in Fisica, Università Cattolica del Sacro Cuore, Brescia

[18] V. Juvé, A. Crut, P. Maioli, M. Pellarin, M. Broyer, N. Del Fatti and F. Vallée *Probing elasticity at the nanoscale: THz acoustic vibrations of nanometric platinum particles*, LASIM, CNRS-Université Lyon 1

[19] A. Crut, V. Juvé, D. Mongin, P. Maioli, N. Del Fatti and F. Vallée (May 26, 2011) *Physical Review B* **83**, 205430 (2011)

[20] V. Juvé, A. Crut, P. Maioli, M. Pellarin, M. Broyer, N. Del Fatti and F. Vallée (2010) *Nano Lett.* **2010**, textit10, 1853-1858, DOI:10.102/nl100604r

[21] H. Lamb (May 11, 1882) *On the vibrations of an elastic sphere*, Proc. London Math. Soc. 13:189

[22] Klaus D. Sattler (September 17, 2010) *Handbook of Nanophysics: Nanoparticles and Quantum Dots*, CRC Press

[23] G. T. Noe II, Q. Zhang, J. Lee; E. Kato, G. L. Woods, H. Nojiri and J. Kono (September 10, 2014) *Rapid scanning terahertz time-domain magnetospectroscopy with a table-top repetitive pulsed magnet*, APPLIED OPTICS, Vol. 53, No. 26

[24] Gregory V. Hartland (March 24, 2011) *Optical Studies of Dynamics in Noble Metal Nanostructures*, Chem. Rev. 2011, 111, 3872

[25] J. Ouellette (February/March 2004) *Time-Resolved Spectroscopy Comes of Age*, American Institute of Physics

[26] A. Assion, M. Geisler, J. Helbing, V. Seyfried and T. Baumert (December 1996) *Femtosecond pump-probe photoelectron spectroscopy: Mapping of vibrational wave-packet motion*, Phis. Rev. A, Vol. 54, No. 6

[27] Thorlabs (2010) *Operation Manual*, Balanced Amplified Photodetectors PDB400 Series

Acknowledgments

Even the writing of thesis, as well as the entire academic career, requires diligence and self-denial. I think they know about the people who share with me these last steps of my path. So I think it is fair to end with a few words of thanks.

First I would like to thank my supervisor, Prof. Gabriele Ferrini, for having suggested me this interesting topic of research and for his teachings, that have made me passionate about this subject. A special thanks also to Simone, who, despite his commitments, has always found time to support me in the lab, solving all the small and large problems that an experimental thesis implies. Thanks to Prof. Francesco Banfi for all the invaluable explanations, and to all the students and teachers of the group ULYSSES.

A thanks goes to the team of researchers of ICRM-CNR in Milan, to Marcella, Chiara and Francesco who have made this work possible with their cooperation.

Thanks to those who, before this experience, has shared with me joys and sorrows of the lab, Paolo and the two Andrea, without whom this last year would not have been the same. Thanks to all the mathematicians, who have proved to be more than simple classmates.

Thanks to my old friends who, despite the years since the first day at Arnaldo, are still here, and thanks to the person who, that day, waited for me outside an office for more than an hour. This is the result of that wait.

A huge THANKS, though, goes to those who have supported my choice from every point of view: to my parents, for the sacrifices they have made in these years and for all the patience that having a daughter like me requires. Give them this little emotion is the only way for me to express my gratitude.

Thanks to my sister, Sara, who, just by her example, has been able to give me great motivations. If you can read your name on this page, it means that even your little sister has grown up.

Thanks also to my only cousin, Nahjla, who, with great joy, was forced to hear me repeat and to suffer my nervousness.

And, finally, knowing how difficult it is to stand by me, a thanks to you, Christian, for surviving eight examination sessions.

Ringraziamenti

Anche la stesura della tesi, così come tutto il percorso universitario, è una fase che richiede impegno e sacrificio. Penso che lo sappiano bene le persone che hanno avuto modo di condividere con me questi ultimi passi del mio cammino. Per questo ritengo che sia doveroso concludere con alcune parole di ringraziamento.

Innanzitutto vorrei ringraziare il Prof. Gabriele Ferrini, mio relatore, per avermi proposto questo interessante argomento di ricerca e per avermi, con i suoi insegnamenti, trasmesso una grande passione per la materia. Un ringraziamento particolare va anche a Simone che, nonostante i suoi impegni, ha sempre trovato il tempo di affiancarmi in laboratorio, risolvendo tutti i piccoli e grandi problemi tecnici che una tesi sperimentale pone. Grazie al prof. Francesco Banfi, per gli innumerevoli, preziosi chiarimenti, e a tutti i ragazzi e docenti del gruppo ULYSSES.

Un grazie va al gruppo di ricercatori dell'ICRM-CNR di Milano, a Marcella, Chiara e Francesco, che, con la loro collaborazione, hanno reso possibile questo lavoro.

Grazie a chi, prima di questa esperienza, ha condiviso con me gioie e dolori del laboratorio, a Paolo e ai due Andrea, senza i quali questo ultimo anno non sarebbe stato lo stesso. Grazie ai matematici e alle matematiche, che si sono rivelati molto più che semplici compagni di corso.

Grazie alle amiche di sempre che, nonostante di anni da quel primo giorno all'Arnaldo ne siano passati, sono ancora qui, e a chi, quel giorno, mi ha aspettato fuori da uno studio per più di un'ora. Questo è il frutto di quell'attesa.

Un enorme GRAZIE, però, va a chi ha supportato, sotto ogni punto di vista, la mia scelta: ai miei genitori, per i sacrifici che hanno fatto in questi anni e per la pazienza che richiede avere una figlia come me. Regalare loro questa piccola emozione è l'unico modo che ho per esprimere tutta la mia gratitudine.

Grazie alla mia sister, Sara, che, semplicemente con il suo esempio, è riuscita a darmi grandi motivazioni. Se puoi leggere il tuo nome su questa pagina significa che anche la tua sorellina è diventata grande.

Grazie anche alla mia unica cuginetta, Nahjla, per avermi, con sua immensa gioia, ascoltato ripetere e per essere stata costretta a subire il mio nervosismo.

Ed, infine, sapendo quanto sia difficile starmi accanto, un ultimo ringraziamento va a te, Christian, per essere sopravvissuto a ben otto sessioni d'esame.